

Numerical Study on GRB-Jet Formation in Collapsars

Shigehiro Nagataki^{1,2}, Rohta Takahashi³, Akira Mizuta⁴, Tomoya Takiwaki⁵

ABSTRACT

Two-dimensional magnetohydrodynamic simulations are performed using the ZEUS-2D code to investigate the dynamics of a collapsar that generates a GRB jet, taking account of realistic equation of state, neutrino cooling and heating processes, magnetic fields, and gravitational force from the central black hole and self gravity. It is found that neutrino heating processes are not so efficient to launch a jet in this study. It is also found that a jet is launched mainly by B_ϕ fields that are amplified by the winding-up effect. However, since the ratio of total energy relative to the rest mass energy in the jet is not so high as several hundred, we conclude that the jets seen in this study are not be a GRB jet. This result suggests that general relativistic effects, which are not included in this study, will be important to generate a GRB jet. Also, the accretion disk with magnetic fields may still play an important role to launch a GRB jet, although a simulation for much longer physical time ($\sim 10 - 100$ s) is required to confirm this effect. It is shown that considerable amount of ^{56}Ni is synthesized in the accretion disk. Thus there will be a possibility for the accretion disk to supply sufficient amount of ^{56}Ni required to explain the luminosity of a hypernova. Also, it is shown that neutron-rich matter due to electron captures with high entropy per baryon is ejected along the polar axis. Moreover, it is found that the electron fraction becomes larger than 0.5 around the polar axis near the black hole by ν_e capture at the region. Thus there will be a possibility that r -process and r/p -process nucleosynthesis occur at these regions. Finally, much neutrons will

¹Yukawa Institute for Theoretical Physics, Kyoto University, Oiwake-cho Kitashirakawa Sakyo-ku, Kyoto 606-8502, Japan, E-mail: nagataki@yukawa.kyoto-u.ac.jp

²KIPAC, Stanford University, P.O.Box 20450, MS 29, Stanford, CA, 94309

³Graduate School of Arts and Sciences, The University of Tokyo, Tokyo 153-8902, Japan

⁴Max-Planck-Institute für Astrophysik, Karl-Schwarzschild-Str. 1, 85741 Garching, Germany

⁵Department of Physics, The University of Tokyo, Bunkyo-ku, Tokyo 113-0033, Japan

be ejected from the jet, which suggests that signals from the neutron decays may be observed as the delayed bump of the light curve of the afterglow or gamma-rays.

Subject headings: gamma rays: bursts — accretion, accretion disks — black hole physics — MHD — supernovae: general — nucleosynthesis

1. INTRODUCTION

There has been growing evidence linking long gamma-ray bursts (GRBs; in this study, we consider only long GRBs, so we refer to long GRBs as GRBs hereafter for simplicity) to the death of massive stars. The host galaxies of GRBs are star-forming galaxies and the positions of GRBs appear to trace the blue light of young stars (Vreeswijk et al. 2001; Bloom et al. 2002; Gorosabel et al. 2003). Also, 'bumps' observed in some afterglows can be naturally explained as contribution of bright supernovae (Bloom et al. 1999; Reichart 1999; Galama et al. 2000; Garnavich et al. 2003). Moreover, direct evidence of some GRBs accompanied by supernovae have been reported such as the association of GRB 980425 with SN 1998bw (Galama et al. 1998; Iwamoto et al. 1998), that of GRB 030329 with SN 2003dh (Hjorth et al. 2000; Price et al. 2003; Stanek et al. 2003), and that of GRB 060218 and SN 2006aj (Mirabal et al. 2006; Mazzali et al. 2006).

It should be noted that these supernovae (except for SN 2006aj) are categorized as a new type of supernovae with large kinetic energy ($\sim 10^{52}$ ergs), nickel mass ($\sim 0.5M_{\odot}$), and luminosity (Iwamoto et al. 1998; Woosley et al. 1999), so these supernovae are sometimes called hypernovae. The total explosion energy of the order of 10^{52} erg is too important to be emphasized, because it is generally considered that a normal core-collapse supernova cannot cause such an energetic explosion. Thus another scenario has to be considered to explain the system of a GRB associated with a hypernova. One of the most promising scenarios is the collapsar scenario (Woosley 1993). In the collapsar scenario, a black hole is formed as a result of gravitational collapse. Also, rotation of the progenitor plays an essential role. Due to the rotation, an accretion disk is formed around the equatorial plane. On the other hand, the matter around the rotation axis freely falls into the black hole. MacFadyen and Woosley (1999) pointed out that the jet-induced explosion along the rotation axis may occur due to the heating through neutrino anti-neutrino pair annihilation that are emitted from the accretion disk (see also Fryer and Mészáros 2000).

It is true that the collapsar scenario is the breakthrough on the problem of the central engine of GRBs. However, there are many effects that have to be involved in order

to establish the scenario firmly. First of all, neutrino heating effects have to be investigated carefully by including microphysics of neutrino processes in the numerical simulations. It is true that MacFadyen and Woosley (1999) have done the numerical simulations of the collapsar, in which a jet is launched along the rotation axis, but detailed microphysics of neutrino heating is not included in their simulations. Secondly, it was pointed out that effects of magnetic fields and rotation may play an important role to launch the GRB jets (Proga et al. 2003; Mizuno et al. 2004a; Mizuno et al. 2004b; Proga 2005; Shibata and Sekiguchi 2005; Sekiguchi and Shibata 2005; Fujimoto et al. 2006), although neutrino heating effects are not included in their works. Recently, Rockefeller et al (2006) presented 3-dimensional simulations of collapsars with smoothed particle hydrodynamics code. In their study, 3-flavor flux-limited diffusion package is used to take into account neutrino cooling and absorption of electron-type neutrinos, although neutrino anti-neutrino pair annihilation is not included. They have shown that alpha-viscosity drives energetic explosion through 3-dimensional instabilities and angular momentum transfer, although the jet is not launched and magnetic fields (source of the viscosity) are not included in their study. Thus it is not clear which effects are most important to launch a GRB jet, that is, what process is essential as the central engine of GRBs.

Due to the motivation mentioned above, we have performed two-dimensional magnetohydrodynamic simulations of collapsars with magnetic fields, rotation, and neutrino cooling/heating processes. In our simulations, the realistic equation of state (EOS) of Blinnikov et al. (1996) and effects of photo-disintegration of nuclei are also included. We investigated influence of magnetic fields on the dynamics of collapsars by changing initial amplitude of the magnetic fields. In section 2, models and numerical methods are explained. Results are shown in section 3. Discussions are described in 4. Summary and conclusion are presented in section 5.

2. MODELS AND NUMERICAL METHODS

Our models and numerical methods of simulations in this study are shown in this section. First we present equations of ideal MHD, then initial and boundary conditions are explained. Micro physics included in this study (equation of state (EOS), nuclear reactions, and neutrino processes) is also explained.

2.1. Magnetohydrodynamics

We have done two-dimensional MHD simulations taking account of self-gravity and gravitational potential of the central point mass. The calculated region corresponds to a quarter of the meridian plane under the assumption of axisymmetry and equatorial symmetry. The spherical mesh with $150(r) \times 30(\theta)$ grid points is used for all the computations. The radial grid is nonuniform, extending from $r = 1.0 \times 10^6$ to 1.0×10^{10} cm with finer grids near the center, while the polar grid is uniform. The minimum radial grid is set to be 3.0×10^5 cm. We have confirmed that a free flow is smoothly solved with this grid resolution.

The basic equations in the following form are finite differenced on the spherical coordinates:

$$\frac{D\rho}{Dt} = -\rho \nabla \cdot \mathbf{v} \quad (1)$$

$$\rho \frac{D\mathbf{v}}{Dt} = -\nabla p - \rho \nabla(\Phi_p + \Phi_s) + \frac{1}{4\pi}(\nabla \times \mathbf{B}) \times \mathbf{B} \quad (2)$$

$$\rho \frac{D}{Dt} \left(\frac{e}{\rho} \right) = -p \nabla \cdot \mathbf{v} - \mathbf{L}_\nu^- + \mathbf{L}_\nu^+ + \mathbf{L}_{\text{nucl}} \quad (3)$$

$$\frac{\partial \mathbf{B}}{\partial t} = \nabla \times (\mathbf{v} \times \mathbf{B}) \quad (4)$$

$$\Delta \Phi_s = 4\pi G \rho \quad (5)$$

$$\frac{DY_e}{Dt} = -Y_p \Gamma_{p \rightarrow n} + Y_n \Gamma_{n \rightarrow p}, \quad (6)$$

where ρ , \mathbf{v} , p , Φ_p , Φ_s , e , L_ν^\pm , L_{nucl} , Y_e , Y_p , Y_n , $\Gamma_{p \rightarrow n}$, and $\Gamma_{n \rightarrow p}$, and are density, velocity, pressure, gravitational potential due to the central point mass (black hole), gravitational potential due to self gravity, internal energy density, heating/cooling rates due to neutrino processes, energy gain (loss) rate due to nuclear reaction, fraction of electron, proton, neutron, and reaction rate from proton to neutron (electron capture rate plus ν_e capture on neutron) and from neutron to proton (positron capture plus $\bar{\nu}_e$ capture on proton), respectively. The Lagrangian derivative is denoted as D/Dt . The gravitational potential of the black hole is modified to take into account some of the general relativistic effects (Paczynski & Witta 1980), $\Phi_p = -GM/(r - r_s)$ where $r_s = 2GM/c^2$ is the Schwartzschild radius. Self-gravity is obtained in ZEUS-2D code developed by Stone and Norman (1992a,b), by solving the matrix which results from finite-differencing the Poisson equation in two dimension. The ZEUS-2D code is also used to solve the MHD equations with second order accurate interpolation in space. Energy gain (loss) rate due to nuclear reaction and heating/cooling rates due to neutrino processes are described in subsections 2.3.2 and 2.3.3. Effects of α -viscosity and (anomalous) resistivity are not included in this study to avoid the uncertainty of the treatment of these effects.

2.2. Initial and Boundary Conditions

We adopt the model E25 in Heger et al. (2000). This model corresponds to a star that has $25M_{\odot}$ initially with solar metallicity, but loses its mass and becomes to be $5.45M_{\odot}$ of a Wolf-Rayet star at the final stage. This model seems to be a good candidate as a progenitor of a GRB since losing their envelope will be suitable to be a Type Ic-like supernova and to make a baryon poor fireball. The mass of the iron core is $1.69M_{\odot}$ in this model. Thus we assume that the iron core has collapsed and formed a black hole at the center. This treatment is same with Proga et al. (2003). The Schwartzschild radius of the black hole is 5.0×10^5 cm initially.

We explain how the angular momentum is distributed initially. At first, we performed 1-D simulation for the spherical collapse of the progenitor for 0.1 s when the inner most Si-layer falls to the inner most boundary ($=10^6$ cm). After the spherical collapse, angular momentum was distributed so as to provide a constant ratio of 0.05 of centrifugal force to the component of gravitational force perpendicular to the rotation axis at all angles and radii, except where that prescription resulted in j_{16} greater than a prescribed maximum value, 10. This treatment is similar to the one in MacFadyen and Woosley (1999). The total initial rotation energy is 2.44×10^{49} erg that corresponds to 1.3×10^{-2} for initial ratio of the rotation energy to the gravitational energy (T/W).

Configuration and amplitude of the magnetic fields in a progenitor prior to collapse are still uncertain. Thus in this study we choose a simple form for the initial configuration prior to collapse and the amplitude is changed parametrically. Initial configuration of the magnetic fields is chosen as follows:

$$\vec{B}(\vec{r}) = \frac{1}{3}B_0 \left(\frac{r_0}{r}\right)^3 (2 \cos \theta \vec{e}_r + \sin \theta \vec{e}_\theta) \quad \text{for } r \geq r_0 \quad (7)$$

$$= \frac{2}{3}B_0(\cos \theta \vec{e}_r - \sin \theta \vec{e}_\theta) \quad \text{for } r < r_0. \quad (8)$$

This configuration represents that the magnetic fields are uniform in a sphere ($r < r_0$), while dipole at outside of the sphere. We set r_0 to be the boundary between CO core/He layer ($= 3.6 \times 10^9$ cm). B_0 corresponds to the strength of the magnetic field in the sphere. We have chosen B_0 to be 0, 10^8 G, 10^9 G, 10^{10} G, 10^{11} G, and 10^{12} G.

As for the boundary condition in the radial direction, we adopt the outflow boundary condition for the inner and outer boundaries. That is, the flow from the central black hole is prohibited at the inner boundary and the inflow from the surface of the progenitor is prohibited at the outer boundary. Of course, the mass of the central black hole becomes larger due to the mass accretion from the inner boundary. As for the boundary condition

in the zenith angle direction, axis of symmetry boundary condition is adopted for the rotation axis, while the reflecting boundary condition is adopted for the equatorial plane. As for the magnetic fields, the equatorial symmetry boundary condition, in which the normal component is continuous and the tangential component is reflected, is adopted.

2.3. Micro Physics

2.3.1. Equation of State

The equation of state (EOS) used in this study is the one developed by Blinnikov et al. (1996). This EOS contains an electron-positron gas with arbitrary degeneracy, which is in thermal equilibrium with blackbody radiation and ideal gas of nuclei. We used the mean atomic weight of nuclei to estimate the ideal gas contribution to the total pressure, although its contribution is negligible relative to those of electron-positron gas and thermal radiation in our simulations.

2.3.2. Nuclear Reactions

Although the ideal gas contribution of nuclei to the total pressure is negligible, effects of energy gain/loss due to nuclear reactions are important. In this study, nuclear statistical equilibrium (NSE) was assumed for the region where $T \geq 5 \times 10^9$ [K] is satisfied. This treatment is based on the assumption that the timescale to reach and maintain NSE is much shorter than the hydrodynamical time. Note that complete Si-burning occurs in explosive nucleosynthesis of core-collapse supernovae for the region $T \geq 5 \times 10^9$ [K] (Thielemann et al. 1996). The hydrodynamical time in this study, \sim s (as shown in Figs 3, 4, and 10, the nuclear reaction occurs at $\sim (10^7 - 10^8)$ cm where the radial velocity is of the order of $(10^7 - 10^8)$ cm s $^{-1}$), is comparable to the explosive nucleosynthesis in core-collapse supernovae, so the assumption of NSE adopted in this study seems to be well. 5 nuclei, n, p, ^4He , ^{16}O , and ^{56}Ni were used to estimate the binding energy of ideal gas of nuclei in NSE for given (ρ, T, Y_e) . Y_e is electron fraction that is obtained from the calculations of neutrino processes in section 2.3.3. On the other hand, we assumed that no nuclear reaction occurs for the region where $T < 5 \times 10^9$ [K].

2.3.3. Neutrino Processes

Neutrino cooling processes due to pair capture on free nucleons, pair annihilation, and plasmon decay are included in this study. Since photoneutrino and bremsstrahlung processes are less important ones at $10^9 < T < 10^{11}$ [K] and $\rho < 10^{12}$ [g cm⁻³] (Itoh et al. 1989) where neutrino cooling effects are important in our calculations, we do not include these processes.

As for the electron capture on free proton, we extend the formulation of Epstein and Pethick (1981) to arbitrary degeneracy. The energy loss rate per proton \dot{Q}_{EC} [GeV s⁻¹ proton⁻¹] is

$$\dot{Q}_{\text{EC}} = \frac{G_\beta^2(C_V^2 + 3G_A^2)}{2\pi^3\hbar} \{ (k_B T)^6 F_5(x) + 2Q_v(k_B T)^5 F_4(x) + Q_v^2(k_B T)^4 F_3(x) \} \quad (9)$$

$$\times \frac{\exp(F_5(\eta)/F_4(\eta))}{1 + \exp(F_5(\eta)/F_4(\eta))},$$

where $G_\beta = G_F \cos \theta_c$ (in units of GeV⁻²) is the Fermi coupling constant (θ_c is the Cabbibo angle), $C_V = 1/2 + 2 \sin^2 \theta_W$ is the vector coupling constant (θ_W is the Weinberg angle), $C_A = 1/2$ is the axial-vector coupling constant, k_B is the Boltzmann constant, and $Q_v = (m_n - m_p)c^2$ is mass difference between neutron and proton. x and η are defined as $x = (\mu_e - Q_v)/(k_B T)$ and $\eta = \mu_e/(k_B T)$, where μ_e is the chemical potential of electrons. $F_i(x)$ is the Fermi integral that is defined as

$$F_i(x) = \int_0^\infty \frac{y^i}{1 + e^{y-x}} dy. \quad (10)$$

We used the formulation derived by Takahashi et al. (1978) to solve the Fermi integral. Note that the leading term becomes the first term in Eq. 10 and obeys $\propto T^6$ when electrons are not degenerated, although other terms dominate when electrons become to be degenerated. We also include the Fermi blocking factor (Herant et al. 1994) due to ν_e assuming that the chemical potential of ν_e is zero and mean energy of the emitted neutrinos by this process is $k_B T F_5(\eta)/F_4(\eta)$ (Rosswog & Liebendörfer 2003). All we have to do is to change μ_e to $-\mu_e$ and Q_v to $-Q_v$ to estimate the positron capture on free neutron. As for the plasmon decays, we used the formulation of Itoh et al. (1989) with the blocking factor (Herant et al. 1994) assuming that the chemical potential of ν_e is zero and mean energy of the emitted neutrinos is $k_B T \{1 + \gamma_{\text{loss}}^2/2(1 + \gamma_{\text{loss}})\}$ where $\gamma_{\text{loss}} = 5.565 \times 10^{-2} \sqrt{\pi^2/3 + \eta^2}$ (Rosswog & Liebendörfer 2003). We have also used the formulation of Itoh et al. (1999) for pair annihilation with the blocking factor (Herant et al. 1994). The mean energies of ν_e and $\bar{\nu}_e$ emitted by this process are $k_B T F_4(\eta)/F_3(\eta)$ and $k_B T F_4(-\eta)/F_3(-\eta)$, respectively (Cooperstein et al. 1986).

In our simulations, density at the inner most region reaches as high as $10^{12} \text{ g cm}^{-3}$ where nuclei are almost photo-disintegrated into nucleons. In this region, as discussed in section 4.1, optically thin limit breaks down. In order to take into account such a high density region, neutrino leakage scheme is introduced (Kotake et al. 2003). In this scheme, we calculate typical diffusion timescale for neutrinos to escape from the system. Since chemical composition is dominated by nucleons at such a high density region, the opacity is mainly determined by scattering and absorption by nucleons for ν_e and $\bar{\nu}_e$ and scattering by nucleons for ν_μ , $\bar{\nu}_\mu$, ν_τ , and $\bar{\nu}_\tau$. The mean free path can be written as

$$\lambda_{\nu_e}^{-1} = \frac{\rho}{m_u} \sigma_{\text{sc}}(\epsilon_{\nu_e}) + \frac{\rho Y_n}{m_u} \sigma_{\text{ab}}(\epsilon_{\nu_e}) \quad \text{for } \nu_e \quad (11)$$

$$\lambda_{\bar{\nu}_e}^{-1} = \frac{\rho}{m_u} \sigma_{\text{sc}}(\epsilon_{\bar{\nu}_e}) + \frac{\rho Y_p}{m_u} \sigma_{\text{ab}}(\epsilon_{\bar{\nu}_e}) \quad \text{for } \bar{\nu}_e \quad (12)$$

$$\lambda_{\nu_x}^{-1} = \frac{\rho}{m_u} \sigma_{\text{sc}}(\epsilon_{\nu_x}) \quad \text{for other flavors} \quad (13)$$

where m_u , σ_{sc} , σ_{ab} , Y_p , Y_n , ϵ_{ν_e} , $\epsilon_{\bar{\nu}_e}$, and ϵ_{ν_x} are the atomic mass unit, scattering cross section by nucleon, absorption cross section by nucleon, mass fraction of proton and neutron, and mean energies of ν_e , $\bar{\nu}_e$, and ν_x . We take the cross sections for these interactions from Bethe (1990). The diffusion timescale is given by

$$\tau_{\text{diff}} = \frac{3\Delta R^2}{\pi^2 c \lambda} \quad (14)$$

where we take $\Delta R = (r\Delta r\Delta\theta)^{1/2}$ as the typical diffusion length. Δr and $r\Delta\theta$ are grid sizes in the radial and polar directions at that point. Neutrino emissivity [$\text{GeV cm}^{-3} \text{ s}^{-1}$] at the point is calculated as

$$f_\nu^{\text{leak}} = f_\nu \times \min\left(1.0, \frac{dt}{\tau_{\text{diff}}}\right) \quad (15)$$

where f_ν and dt are neutrino emissivity obtained by the optically thin limit and time step of the simulations. On the other hand, when we estimate the neutrino heating rate, we take optically thin limit for all the regions for simplicity. This corresponds to that we estimate the upper limit for the neutrino heating effects. Even this limit, as shown later, jet like explosion does not occur by the neutrino heating (as shown in Fig. 1). Also, this optically thin limit will be justified since neutrino cooling rate dominates heating rate, as shown in Fig. 8. Detailed discussion on this point is presented in section 4.1.

Neutrino heating process due to neutrino pair annihilation and ν_e and $\bar{\nu}_e$ captures on free nucleons with blocking factors of electrons and positrons are included in this study. As for the neutrino pair annihilation process, the formulation of Goodman et al. (1987) (with

blocking factors) is adopted. The ν_e and $\bar{\nu}_e$ captures on free nucleons are inverse processes of electron/positron captures. The calculation of neutrino heating is the most expensive in the simulation of this study. Thus, to save the CPU time, the neutrino heating processes are calculated only within the limited regions ($r < 10^9$ cm). Moreover, we adopt some criterions as follows in order to save CPU time. We have to determine the energy deposition regions and emission regions to estimate the neutrino heating rate. As for the neutrino pair annihilation process, We adopt no criterion for the energy deposition regions other than $r < 10^9$ cm, while the emission regions satisfy the criterion of $T \geq 3 \times 10^9$ K. As for the neutrino capture process, we adopt the criterions as follows: The absorption regions should satisfy the criterion of $\rho \geq 10^4$ g cm $^{-3}$, while the emission regions satisfy the criterion of (i) $\rho \geq 10^3$ g cm $^{-3}$ and (ii) $T \geq 10^9$ K. Also, these heating rate had to be updated every 100 time steps to save CPU time. Of course this treatment has to be improved in the future. However, this treatment seems to be justified as follows: The total time step is of the order of 10^6 steps. The final physical time is of the order of seconds, so the typical time step is $\sim 10^{-6}$ s. This means that heating rate is updated every $\sim 10^{-4}$ s, which will be shorter than the typical dynamical timescale. This point is discussed in detail in section 4.1

The heating process of neutrino pair annihilation are calculated as follows. Let points A and B be in the emission regions and a point C be in the energy deposition regions. Let d_A , d_B , and d_C be distances between A and B, B and C, and C and A, respectively. The angle ψ is defined as the angle ACB. The energy deposition rate at C, $\dot{Q}(C)$ [GeV cm $^{-3}$ s $^{-1}$], is given formally by integrating the emission regions as

$$\dot{Q}(C) = \frac{KG_F^2}{2\pi c} \int \int dx_A^3 dx_B^3 \frac{(1 - \cos \psi)^2}{d_A^2 d_B^2} \int d\epsilon_\nu d\epsilon_{\bar{\nu}} \epsilon_\nu \epsilon_{\bar{\nu}} (\epsilon_\nu + \epsilon_{\bar{\nu}}) F_\nu F_{\bar{\nu}} (1 - f_e^-)(1 - f_e^+), \quad (16)$$

where K is $(1 - 4 \sin^2 \theta_W + 8 \sin^4 \theta_W)/(6\pi)$ for $\nu_\mu \nu_{\bar{\mu}}$ and $\nu_\tau \nu_{\bar{\tau}}$ annihilation and $(1 + 4 \sin^2 \theta_W + 8 \sin^4 \theta_W)/(6\pi)$ for $\nu_e \nu_{\bar{e}}$ annihilation (Goodman et al. 1987), \mathbf{x}_A and \mathbf{x}_B are locations of the points A and B, $\epsilon_{\nu, \bar{\nu}}$ are energies of (anti-)neutrinos, $F_{\nu, \bar{\nu}}$ are energy spectrum [cm $^{-3}$ s $^{-1}$ GeV $^{-1}$] of (anti-)neutrinos, and f_e^\pm are Fermi blocking factors of electrons/positrons at point C. In this formulation, G_F is written in units of cm GeV $^{-1}$. It is easily seen that Eq. (16) is eight dimensional integral and it takes too much time to accomplish this integral. Thus we have approximated that each neutrino energy spectrum due to each emission process is a monotonic one, that is, we assumed only neutrinos with average energy are emitted when Eq. (16) is carried out. Since the energy loss rate [GeV cm $^{-3}$ s $^{-1}$] is obtained from the formulations of neutrino cooling process mentioned above, number of emitted neutrinos for each process is calculated by dividing the average energy of emitted neutrinos for the process. Although the calculated region is a quarter of the meridian plane, the neutrino flux from the south hemisphere is included assuming the symmetry relative to the equatorial plane. The same treatment with neutrino pair annihilation process is adopted to estimate the

heating rate due to ν_e and $\bar{\nu}_e$ capture processes, that is, average energy of (anti-)electron-type neutrinos is used.

Neutrinos are emitted isotropically in the fluid-rest frame, so strictly speaking, neutrinos are emitted unisotropically in the coordinate system due to the beaming effect (Rybicki and Lightman 1979). In fact, the angular frequency is found to become as large as 10^4 s^{-1} at the inner most region (Figs. 3 and 10) and the rotation velocity, v_ϕ reaches $\sim 10^{10} \text{ cm s}^{-1}$ at most. Thus the beaming effect may be important although we did not take into account the effect in this study.

Finally the models considered in this study are summarized in Table 1. The digit in the name of each model represents the power index of B_0 .

3. RESULTS

We present results of numerical simulations in this section. First of all, we show in Fig 1 the density contour of the central region of the progenitor ($r \leq 10^8 \text{ cm}$) with velocity fields for model 0 and model 9. In the top panels, density contour with velocity fields for model 0 at $t = 2.1 \text{ s}$ (left panel) and $t = 2.2 \text{ s}$ (right panel) is shown, while in the bottom panels the ones for model 9 is shown. The color represents the density (g cm^{-3}) in logarithmic scale ($10^3 - 10^{12}$). Vertical axis and horizontal axis represent polar axis (= rotation axis) and equatorial plane, respectively. You can easily find that a jet is launched at $t = 2.1 \text{ s}$ for model 9, while no jet occurs for model 0. In the following subsections, we explain the dynamics of these models in detail.

3.1. Dynamics without Magnetic Fields

In this subsection, we mainly explain the dynamics of model 0, then the one of model 9 is explained in the next subsection. First, we show the accreted energy and mass accretion rate as a function of time in Fig. 2(a). Solid, short-dashed, and dotted lines represent accreted total energy, kinetic energy, and thermal energy ($\times 10^{50} \text{ erg}$) into the black hole. Long-dashed line represents the mass accretion rate ($M_\odot \text{ s}^{-1}$) as a function of time. From this figure, we can understand the following points: (i) the accreted energy amounts to of the order of 10^{52} erg , which is comparable to the explosion energy of a hypernova. Thus there is a possibility for the models in this study to explain the large explosion energy of a hypernova as long as the released gravitational energy is efficiently converted to the explosion energy. (ii) kinetic energy dominates thermal energy at the inner boundary. This is because almost all thermal

energy is extracted in the form of neutrinos, which is seen in Fig. 6(a). (iii) mass accretion rate drops almost monotonically from $\sim 10^{-1}M_{\odot} \text{ s}^{-1}$ to $\sim 10^{-3}M_{\odot} \text{ s}^{-1}$, which is discussed in sections 3.2 and 4.2.

Next, we show in Fig. 3 profiles of physical quanta of the accretion disk around the equatorial plane. Profiles of density, absolute value of radial velocity, angular frequency, temperature, density scale height, and specific angular momentum in the accretion disk are shown for model 0 at $t = 2.2 \text{ s}$. From the figure, we can understand the following points: (i) the density reaches as high as $10^{12} \text{ g cm}^{-3}$ around the central region. (ii) the inflow velocity (v_r) becomes as low as 10^6 cm s^{-1} at the central region, by which the mass accretion rate becomes as low as $10^{-3}M_{\odot} \text{ s}^{-1}$, as shown in Fig. 2(a) (Note that the mass accretion mainly comes from the region between the rotational axis and the disk. See also Igumenshchev and Abramowicz 2000; Proga and Begelman 2003).

We show in Fig. 4 profiles of mass fraction for nuclear elements at the equatorial plane for model 0 at $t = 2.2 \text{ s}$. Dot-dashed, dotted, short-dashed, long-dashed, and solid lines represent mass fraction of n, p, ^4He , ^{16}O , and ^{56}Ni , respectively. From this figure, we can easily see that oxygen is photo-dissociated into helium at $2 \times 10^8 \text{ cm}$, while helium is photo-dissociated into nucleons at $3 \times 10^7 \text{ cm}$. It is also noted, some ^{56}Ni is seen at $r \leq 3 \times 10^7 \text{ cm}$ (solid line), which may explain the luminosity of a hypernova as long as it is ejected. This point is discussed in section 4.3. The discontinuity of temperature at $3 \times 10^7 \text{ cm}$ in Fig. 3 will come from the cooling effect due to the photo-disintegration of helium into nucleons.

From now on we show the results on neutrino processes. In Fig. 5, we show contour of neutrino cooling rate with velocity fields for model 0 at $t = 2.2 \text{ s}$. The color represents the emissivity of neutrinos ($\text{erg cm}^{-3} \text{ s}^{-1}$) in logarithmic scale ($10^{10} - 10^{34}$). This emissivity of neutrinos is almost explained by pair-captures on free nucleons, as shown in Fig. 6. We can easily see that emissivity of neutrinos is high at the region where the accretion disk is formed.

We show the results on neutrino cooling for every neutrino process. We show in Fig. 6(a) cumulative energy ($\times 10^{50} \text{ erg}$) of emitted neutrinos for each process as a function of time for model 0. Dot-dashed, long-dashed, solid, short-dashed, and dotted lines represent plasmon decay, electron-positron pair annihilation, positron capture, electron capture, and summation of all processes. It is clearly seen that almost all emitted energy comes from pair captures on free nucleons. Also, the emitted energy amounts to of the order of 10^{52} erg (strictly speaking, $3.44 \times 10^{52} \text{ erg}$), which is comparable to the accreted kinetic energy and much higher than the accreted thermal energy (see Fig. 2(a)). Thus we consider that almost all thermal energy, which was comparable to the kinetic energy in the accretion disk, is extracted by neutrino emission. Note that time evolution of electron fraction is mainly determined by positron and

electron capture processes in the accretion disk.

In Fig. 7, we show contour of neutrino heating rate with velocity fields for model 0 at $t = 2.2$ s. The color represents the energy deposition rate ($\text{erg cm}^{-3} \text{s}^{-1}$) in logarithmic scale ($10^{10} - 10^{34}$). Left panel shows the energy deposition rate due to ν_e and $\bar{\nu}_e$ captures on free nucleons, while right panel shows the energy deposition rate due to ν and $\bar{\nu}$ pair annihilation. In the pair annihilation, contributions from three flavors are taken into account. It is, of course, that contour of energy deposition rate due to ν_e and $\bar{\nu}_e$ captures traces the number density of free nucleons, so the energy deposition rate is high around the equatorial plane where the accretion disk is formed. On the other hand, energy deposition rate due to ν and $\bar{\nu}$ pair annihilation occurs everywhere, including the region around the polar axis. This feature will be good to launch a jet along the polar axis, as pointed by MacFadyen and Woosley (1999). However, this heating effect is too low to launch a jet in this study (see Fig. 1).

In Fig. 8(a), we show neutrino luminosity (solid line), energy deposition rate due to ν and $\bar{\nu}$ pair annihilation (dotted line), and energy deposition rate due to ν_e and $\bar{\nu}_e$ captures on free nucleons (dashed line) as a function of time for model 0. It is clearly seen that energy deposition rate is much smaller than the neutrino luminosity, which supports our assumption that the system is almost optically thin to neutrinos. Also, we can see that ν_e and $\bar{\nu}_e$ captures on free nucleons dominates ν and $\bar{\nu}$ pair annihilation process as the heating process. It is also noted that neutrino luminosity and energy deposition rate decreases along with time, which reflects that the mass accretion rate also decreases along with time (Fig. 2(a)).

Finally, we show in Fig. 9(a) the integrated deposited energy ($\times 10^{50}$ erg) due to ν and $\bar{\nu}$ pair annihilation (solid line) and ν_e and $\bar{\nu}_e$ captures on free nucleons (dashed line) as a function of time. It is confirmed that ν_e and $\bar{\nu}_e$ captures on free nucleons dominate ν and $\bar{\nu}$ pair annihilation process as the heating process. However, as shown in Figs. 5 and 7, ν_e and $\bar{\nu}_e$ captures on free nucleons occur mainly in the accretion disk, where neutrino cooling effect dominates neutrino heating effect. Thus ν_e and $\bar{\nu}_e$ captures on free nucleons is not considered to work for launching a jet. As for the ν and $\bar{\nu}$ pair annihilation process, although this process deposit energy everywhere, including the region around the polar axis, the deposited energy amounts to only of the order of 10^{49} erg. This is 10^{-3} times smaller than the explosion energy of a hypernova. In fact, as shown in Fig. 1, the jet is not launched in model 0. Thus we conclude that the efficiency of neutrino heating is too low to launch a jet in this study.

3.2. Dynamics with Magnetic Fields

In this subsection, we explain the dynamics of model 9 as an example of a collapsar with magnetic fields. Dependence of dynamics on the initial amplitude of magnetic fields is shown in section 3.3.1.

First, the accreted energy and mass accretion rate as a function of time are shown in Fig. 2(b). The meaning of each line is same with Fig. 2(a), although dot-dashed line, which is not in Fig. 2 (a), represents accreted electro-magnetic energy ($\times 10^{50}$ erg) into the black hole as a function of time. The reason why the final time of the simulation for model 9 is 2.23 s is that the amplitude of the magnetic field (in particular, B_ϕ) becomes so high at the inner most region that the Alfvén crossing time at the region make the time step extremely small. Also, it seems that the mass accretion rate does not decrease so much in model 9. Rather, it seems to keep $\sim 0.05 M_\odot \text{ s}^{-1}$. We guess this is because magnetic fields play a role to transfer the angular momentum from inner region to outer region, which makes matter fall into the black hole more efficiently. This point is also discussed with Figs. 8–12.

Next, we show in Fig. 10 profiles of physical quanta of the accretion disk around the equatorial plane for model 9 at $t = 2.2$ s. When we compare these profiles with the ones in Fig. 3, we can see that the radial velocity is higher in model 9 at small radius. This may reflect that the mass accretion rate is higher in model 9 than model 0 (as stated in section 3.1, the mass accretion mainly comes from the region between the rotational axis and the torus. So we have to note that this feature does not explain the mass accretion rate directly. see also Fujimoto et al. 2006). As for the other profiles, there seems no significant difference between the two models.

In Fig. 11, we show profiles of amplitude of magnetic fields as a function of radius on the equatorial plane for model 9 at $t = 2.2$ s. Dotted, solid, and dashed lines represent the amplitude of B_r , B_θ , and B_ϕ , respectively. It is clearly seen that B_ϕ dominates within $r = 10^8 \text{ cm}$. Thus we can conclude that magnetic pressure from B_ϕ drives the jet along the rotation axis (see Fig. 1). This point is also discussed with Figs. 13–15. Also, these magnetic fields may play a role to transfer the angular momentum. Since the viscosity parameter α can be estimated as (Balbus & Hawley 1998; Akiyama et al. 2003)

$$\alpha \sim \frac{B_r B_\phi}{4\pi P}, \quad (17)$$

we plot in Fig. 11 the estimated viscosity parameter ($\times 10^{-20}$) (long-dashed line). This figure suggests that α -viscosity coming from the magnetic fields may play a role to transfer the angular momentum at inner most region effectively. However, the angular momentum cannot be transferred to infinity along the radial direction. This is confirmed by the Alfvén Mach

number ($\times 10^{-10}$) in the radial direction ($\equiv v_r/v_{r,A}$; dot-dashed line in Fig. 11). At only the inner most region, the flow becomes marginally sub-Alfvénic where the viscous force due to magnetic stress can bring the angular momentum outward. Thus we consider that the outflow (including the jet) in the polar direction (see Fig. 1 bottom) should bring the angular momentum from the inner most region.

As additional information, we found that the velocity of the slow magnetosonic wave is almost same with the Alfvén velocity. On the other hand, we found that the fluid is subsonic against the fast magnetosonic wave in the simulated region.

We show in Fig. 12 the profiles of specific angular momentum ($\text{cm}^2 \text{s}^{-1}$) on the equatorial plane for model 0 (dotted line) and model 9 (short-dashed line) at $t = 2.2$ s. The profiles of angular momentum density ($\text{g cm}^{-1} \text{s}^{-1}$) for model 0 (long-dashed line) and model 9 (solid line) are also shown in the figure. We confirmed that the specific angular momentum is not so different between model 0 and model 9, but it is found that the angular momentum density is lower in model 9 compared with model 0 at the inner region. This feature might reflect that the matter falls into the black hole efficiently in model 9 at small radius (see Fig. 11). This picture seems to be consistent with the almost constant accretion rate in model 9 (Figs. 2(b)).

Cumulative energy ($\times 10^{50}$ erg) of emitted neutrinos for each process as a function of time for model 9 is shown in Fig. 6(b), neutrino luminosity, energy deposition rate due to ν and $\bar{\nu}$ pair annihilation, and energy deposition rate due to ν_e and $\bar{\nu}_e$ captures on free nucleons as a function of time for model 9 are shown in Fig. 8(b), and integrated deposited energy due to ν and $\bar{\nu}$ pair annihilation and ν_e and $\bar{\nu}_e$ captures on free nucleons as a function of time for model 9 are shown in Fig. 9(b). The meaning of each line in each figure is same with the one used for model 0. We can derive a similar conclusion for the role of neutrino heating effect in model 9 as in model 0. As for the ν_e and $\bar{\nu}_e$ captures on free nucleons, the cumulative deposited energy becomes as high as 10^{52} ergs that is comparable to the explosion energy of a hypernova. However, this heating process occurs mainly in the accretion disk, where neutrino cooling effect dominates neutrino heating effect. Thus ν_e and $\bar{\nu}_e$ captures on free nucleons is not considered to work for launching a jet. As for the ν and $\bar{\nu}$ pair annihilation process, the deposited energy amounts to no more than 10^{50} erg. Thus we conclude that the neutrino heating effect in model 9 is too inefficient to launch a GRB jet and cause a hypernova. It has to be noted that the energy deposition rate due to pair captures on free nucleon sometimes becomes larger than the neutrino luminosity in Fig. 8(b). This means that the optically thin limit breaks down at that time. This point is also discussed in section 4.1. We also found that the neutrino luminosity, energy deposition rate, and integrated deposited energy seem to be higher in model 9 than in model 0. We consider that this feature comes from

the high mass accretion rate (high rate of release of gravitational energy) caused by angular momentum transfer due to magnetic fields.

We show in Fig. 13 time evolution of energy of magnetic fields ($\times 10^{50}$ erg) in the whole calculated region for the case of model 9. Dotted, solid, and dashed lines represent energy in the form of B_r , B_θ , and B_ϕ , respectively. We can see that B_ϕ grows rapidly and dominates other components, although B_ϕ is much smaller than other components at first (note that 1-D simulation of the spherical collapse of the progenitor is done until $t = 0.1$ s (see section 2.2), so B_ϕ is set to be 0 until $t = 0.1$ s). B_ϕ is amplified by winding effect and launches a jet along the polar axis (see Fig. 1). The total energy of B_ϕ at the final stage of the simulation in this study is of the order of 10^{50} erg, which is much smaller than the explosion energy of a hypernova. However, the total energy of B_ϕ is increasing almost monotonically. As mentioned above, the final time of the simulation for model 9 is determined due to the reason that the Alfvén crossing time becomes extremely small at the inner most region. When we can overcome this problem and simulate the model 9 further, there is a possibility that the energy of B_ϕ becomes comparable to the explosion energy of a hypernova. The evolution of B_r and B_θ is similar to the one by Magnetic Rotational Instability (MRI), which is discussed in section 4.2.

We show in Fig. 14 contour of plasma beta ($=p_{\text{gas+radiation}}/p_{\text{mag}}$) with magnetic fields (B_r and B_θ) for model 9 at $t = 2.2$ s. In $p_{\text{gas+radiation}}$, degenerated pressure of electrons is included. The color represents the plasma beta in logarithmic scale ($10^{-1} - 10^8$). The minimum value of plasma beta in this region is 0.193. We can see clearly that the beta value is low in the jet region, from which we can understand the jet is launched by the magnetic fields (in particular, B_ϕ).

Finally, we have performed these simulations presented in sections 3.1 and 3.2 without calculating self-gravity, and found that the dynamics of the collapsar is not changed so much.

3.3. Toward Discussions

Before we discuss the results mentioned above, we present two more results in this section. One is the dependence of dynamics on initial amplitude of magnetic fields, the other is the explosive nucleosynthesis.

3.3.1. Dependence on Initial Amplitude of Magnetic Fields and on Resolution of Grids

Here we show the dependence of dynamics on initial amplitude of magnetic fields. In Fig. 15, evolutions of total energy of magnetic fields ($\times 10^{50}$ erg) for model 8 (top-left panel), model 10 (top-right panel), model 11 (bottom-left panel), and model 12 (bottom right panel) are shown. The final time of the simulation is determined, like in model 9, by the reason that the Alfvén crossing time becomes extremely small at the inner most region. In all models, the energy of B_ϕ amounts to $10^{49} - 10^{50}$ erg, which means that the amplitude of B_ϕ becomes as strong as 10^{15} G. This can be understood by simple calculations: the typical radius of the inner most region is of the order of 10^6 cm, so the volume of the region times the energy density of magnetic fields becomes $E_B = 8.3 \times 10^{49} (B/2 \times 10^{15} \text{ G})^2 (r/5 \times 10^6 \text{ cm})^3$ erg.

The total energy of B_r and B_θ components does not change so much with time. In particular, in models 10–12, their total energy hardly changes. When we compare B_r with B_θ , B_r seems to be more unstable than B_θ (see also Fig. 13). This is similar to the results of the local simulations of MRI, which is discussed in section 4.2.

We summarize the features of the launched jet at the final stage of simulations for every model in Table 2. We define the jet as follows: (i) the region within some opening angle (θ_j) (ii) the region where total energy (i.e. summation of kinetic, thermal, electro-magnetic, and gravitational energies) is positive at the final stage of the simulations. (iii) the amplitude of the velocity is larger than 5×10^9 cm s $^{-1}$. In Table 2, total energy, mass, terminal bulk Lorentz factor, and ratio of the magnetic energy relative to total energy of the jet is shown assuming that $\theta_j = 5^\circ, 10^\circ$, and 15° for each model. Terminal bulk Lorentz factor is estimated by assuming that total energy goes into kinetic energy during expansion.

We can see that terminal bulk Lorentz factor in every model is much smaller than the required value (~ 300) for GRB jets. Also, the energy of the jet in every model is much smaller than the typical energy of a GRB. Thus we conclude that the jets seen in this study will not be GRB jets.

Also, we show in left panel of Fig. 16 the evolution of total energy of magnetic fields for the case of model 9 (same with Fig. 13), but for $150(r) \times 5(\theta)$ grid points (left panel) and $150(r) \times 20(\theta)$ grid points (right panel) to show the dependence of results on the grid resolution. It is found that the growth rate of B_r and B_θ components depends on the grid resolution. On the other hand the growth rate of B_ϕ does not depend on the grid resolution (that is, the energy in B_ϕ fields becomes $10^{49} - 10^{50}$ ergs in (1-2) sec). The saturation level of B_r and B_θ does not depend on the grid resolution so much. This is discussed in section 4.2. We have also done a simulation of model 9 with finer resolution ($300(r) \times 60(\theta)$), although neutrino anti-neutrino pair annihilation is not included to save CPU time. The simulation

region is set to be ($10^6 \text{ cm} \leq r \leq 10^9 \text{ cm}$, $0 \leq \theta \leq 90$). The minimum radial grid is set to be $3 \times 10^5 \text{ cm}$. We have found that the dynamics of collapsars is hardly changed. We have found that an accretion disk is formed around the black hole and a jet is launched at $t = 1.98 \text{ sec}$. Moreover, we have found that the evolution of magnetic fields is hardly changed, which is shown in right panel of Fig. 16. This result means that a jet is driven by magnetic fields and the standard resolution of our study ($150(r) \times 30(\theta)$) is not so bad.

3.3.2. Nucleosynthesis

In this section, we present results on explosive nucleosynthesis. We show in Table 3 the mass of ^{56}Ni in the regions where total energy is positive ($M_{\text{Ni}}^{\text{esc}} (M_{\odot})$) and the total mass of ^{56}Ni in the whole simulated region ($M_{\text{Ni}}^{\text{tot}} (M_{\odot})$) for each model. These amounts are estimated at the final stage of the simulations. The ejected mass of ^{56}Ni , $M_{\text{Ni}}^{\text{esc}}$, is too little to explain the luminosity of a hypernova, although considerable amount of ^{56}Ni is synthesized in the accretion disk ($M_{\text{Ni}}^{\text{tot}} (M_{\odot})$). We found that the ejected mass is mainly composed of n , p , and He. This is supported by Fig. 17 where entropy per baryon at $t = 2.2 \text{ s}$ for model 9 is shown in units of k_b . In the jet region, the entropy per baryon is remarkably high, so it is natural that light elements dominate in the jet region.

Finally, we show in Fig. 18 contour of electron fraction (Y_e) with velocity fields for model 0 at $t = 2.2 \text{ s}$ (left panel) and model 9 at $t = 2.2 \text{ s}$ (right panel). The color represents the electron fraction on a linear scale (0.1-0.540). We can easily see that Y_e becomes low in the accretion disk. This is because electrons are degenerated and electron capture dominates positron capture at this region. Also, we can see that mass element with low Y_e is ejected in model 9. Also, mass element with high Y_e (highest value is 0.522) is also ejected in model 9 from the inside of the low Y_e jet along the polar axis near the black hole.

Since entropy per baryon is very high in the jet region (Fig. 17), these mass elements may cause r -process and/or r/p -process nucleosynthesis. Here we have to comment on the electron fraction at the high density region. The value of the electron fraction is solved of the order of 0.1 in the accretion disk. This value is obtained assuming that the chemical potential of electron-type neutrinos is zero. If careful treatment of neutrino transfer is done, the chemical potential of electron-type neutrinos may prohibit the electron fraction from being as low as 0.1. This point is discussed in sections 4.1 and 4.3.

4. DISCUSSIONS

In this section, we discuss our numerical results and prospect for future works. We discuss neutrino physics, effects of magnetic fields, nucleosynthesis, general relativistic effects, initial conditions, and prospect for improvements of our numerical code.

4.1. Neutrino Physics

In this study, we found that deposited energy due to neutrino pair annihilation are too small to explain the explosion energy of a hypernova and a GRB (Fig. 9). Even though the deposited energy by electron-type neutrino capture on free nucleons can be comparable to the explosion energy of a hypernova in model 9 (Fig. 9), the deposition region is the high density region (Fig. 7) where cooling effect dominates the heating effect (Fig. 5). In particular, no jet was found in the numerical simulations of model 0 (Fig. 1). The energetics of this system can be understood from Figs. 2, 6, and 9. The released gravitational energy by collapse is the energy source of accreted energy and neutrinos. From Figs. 2 and 6, we can understand that the kinetic energy and thermal energy share the released gravitational energy almost equally, then almost thermal energy was extracted in the form of neutrinos. The total energies of accreted energy and neutrinos are of the order of 10^{52} erg, then the emitted neutrino energy was deposited into matter through weak interactions. Its efficiency is less than 1% for neutrino pair annihilation, as can be seen in Figs. 6 and 9. As for the efficiency of electron-type neutrino capture it amounts to $\sim 10 - 20\%$. This means that the inner most region of the accretion disk becomes to optically thick against neutrinos and $\sim 10 - 20\%$ of neutrinos are absorbed.

The deposited energy by neutrino pair annihilation is of the order of $(10^{49} - 10^{50})$ erg, which is much smaller than the explosion energy of a hypernova and a GRB. In order to enhance the deposited energy by neutrino pair annihilation, there will be two ways. One is to enhance the released gravitational energy, the other is to enhance the efficiency of energy deposition. The former corresponds to enhance the mass accretion rate, which will be realized if effective angular momentum transfer is realized. From Figs. 2, 8, and 12, it was inferred that magnetic fields seem to work efficiently so that high mass accretion rate is realized. Of course, the mass accretion rate also depends on the distribution of initial angular momentum. We should investigate these effects further in the future. As for the efficiency of energy deposition, it will be enhanced when the general relativistic effects are taken into account. This is because neutrinos are trapped around the black hole, so that the possibilities of neutrino pair annihilation and neutrino capture become enhanced. This effect is investigated in detail by using a steady solution of an accretion disk in the forth-coming

paper. Of course, we are planning to include this effect in our numerical code in the future.

Although we believe that our conclusion on the energetics mentioned above will be unchanged, we have to improve our treatment on the neutrino heating for further study. In this study, we took the optical thin limit to estimate the neutrino heating rate. This will be justified by Figs. 6 and 9. However, for further study, we have to investigate the cases in which mass accretion rate is higher than in this study to achieve energetic explosion enough to explain the explosion energies of a hypernova and a GRB. In fact, we consider that the optically thin limit breaks down even the models in this study at the highest density region. This is estimated as follows: The cross section of ν_e and $\bar{\nu}_e$ captures on free nucleons is given by $\sigma \sim \sigma_0(\epsilon_\nu/m_e c^2)^2$ where $\sigma_0 = 1.76 \times 10^{-44} \text{ cm}^2$. Since the highest density in the accretion disk is of the order of $10^{12} \text{ g cm}^{-3}$ at $r \sim 10^6 \text{ cm}$ (the scale height is also of the order of 10^6 cm) and typical energy of neutrinos are of the order of 10 MeV (see Figs. 3 and 10), the optical depth at this region is $\tau = \sigma(\rho/m_p)L \sim 4.2(\epsilon_\nu/10\text{MeV})^2(\rho/10^{12}\text{g cm}^{-3})(L/10^6\text{cm})$. Thus, at the highest density region, the optically thin limit must break down. This picture is also confirmed in Fig. 8(b). In Fig. 8(b), as stated in section 3.2, the energy deposition rate due to pair captures on free nucleon sometimes becomes larger than the neutrino luminosity. This reflects that the optically thin limit breaks down at that time. Although we believe that our conclusion on the energetics will not be changed so much, we are planning to develop the careful neutrino transfer code that includes emissions, absorptions, and scattering of neutrinos for further study. We also note four points that have to be improved for the treatments of neutrino heating. One is that we did not take into account the light-crossing time of the system and assumed that the system is almost steady during the light-crossing time when we estimate the neutrino heating rate. From Figs. 5 and 7, the neutrino cooling and heating occur efficiently within several times of 10^7 cm . Thus the typical light crossing time will be of the order of 1ms. For comparison, the rotation period at the inner most region is $\sim 6.3 \times 10^{-4} \text{ s}$. Since the system forms an accretion disk and the viscosity parameter α is 0.1 at most (Fig. 11), the system will be treated steady at least ten times of the rotation period, $6.3 \times 10^{-3} \text{ s}$. Thus the treatment to neglect the light crossing time will be fairly justified. Second is that we update the neutrino heating rate every 100 timesteps to save the CPU time. The inner most radius is set to be 10^6 cm , so the typical time step is estimated to be $10^6 \times \Delta\theta/c \text{ s}$, where c is the speed of light and $\Delta\theta = \pi/60$. Thus 100 time steps corresponds to $1.74 \sim 10^{-4} \text{ s}$, which will be comparable to free-fall timescale ($\tau_{\text{ff}} = 1/\sqrt{24\pi G\rho} \sim 4.5 \times 10^{-4}(10^{12}\text{g cm}^{-3}/\rho)^{1/2} \text{ s}$ (Woosley 1986)) and rotation period. Thus we believe that this treatment will be fairly justified. Third, we have approximated that each neutrino energy spectrum due to each emission process is monotonic, that is, we assumed only neutrinos with average energy are emitted when Eq. (16) is carried out. However, the cross section of neutrino pair annihilation is proportional to square of the total

energy in the center of mass, and that for electron-type neutrino absorption on free nucleons is proportional to square of neutrino's energy. Thus the contribution of neutrinos with high energy will enhance the efficiency of neutrino heating. These points will be improved when we can include a careful neutrino transfer code in future. The last point is related with the nuclear reactions. In this study, the NSE was assumed for the region where $T \geq 5 \times 10^9$ [K]. Thus, the reactions to maintain NSE occur suddenly when the temperature becomes so high as to satisfy the criterion. However, in reality, NSE might break down at low density region, where cooling effect due to photo-disintegration will be not so strong as in this simulation. It should be also noted that the photo-dissociation from He into nucleons is strong cooling effect and absorb thermal energy when this reaction is switched on. Thus the thermal energy suddenly absorbed by nuclear reactions. That is seen as the discontinuities of temperature in Figs. 3 and 10. Although we believe these discontinuities do not change our conclusion on the energetics mentioned above (because much more neutrinos come from the inner region; Fig. 5), the profile of temperature will be solved smoothly when we use a nuclear reaction network instead of using the NSE relation. Since the emissivity of neutrinos depends very sensitively on the temperature (Bethe 1990; Herant et al. 1992; Lee & Ramirez-Ruiz 2006), estimation of temperature should be treated carefully. We are planning to check the dependence of temperature on the nuclear reaction network and several EOS in the forth coming paper.

Finally, we discuss the detectability of neutrinos from collapsars. Since the event rate is much smaller than the normal core-collapse supernova, the chance probability to detect neutrino signals from a collapsar will be very small. However, if it occurs nearby our galaxy, the neutrino signal from a collapsar will be distinguished from normal core-collapse supernova. As for the normal core-collapse supernovae, the time evolution of the luminosity of neutrino of each flavor is determined firmly by the binding energy of a neutron star and opacity of neutron star against neutrinos. On the other hand, in the case of a collapsar, the time evolution of neutrino luminosity will depend on the time evolution of mass accretion rate, which in turn should depend on the initial distribution of angular momentum and magnetic fields. Thus there should be much varieties of time evolution for the luminosity of neutrinos in the case of collapsars. Also, in the case of collapsars, the dominant process to generate neutrinos is pair captures on free nucleons (see Fig. 6), so in the case of a collapsar, the electron-type neutrinos will be much more produced compared with other flavors. This is in contrast with the normal core-collapse supernovae (e.g. Buras et al. 2006, and see references therein). Of course, we have to take vacuum and matter oscillation effects into account to estimate the spectrum of neutrinos from a collapsar precisely. In particular, in the case of a collapsar, the density distribution is far from spherically symmetric, so we have to be careful about viewing angle to estimate the matter oscillation effect. It is true that the event rate

of collapsars is smaller than normal core collapse supernovae, but the released gravitational energy can be larger if considerable amount of mass of the progenitor falls into the central black hole (Nagataki et al. 2002). Thus we consider that there will be also a possibility to detect a neutrino background from collapsars.

4.2. Effects of Magnetic Fields

We have seen that the mass accretion rate seems to be enhanced in model 9, compared with model 0 (Fig. 2), which enhances the luminosity of neutrinos (Fig. 6) and energy deposition rate due to weak interactions (Fig. 8). This seems to be because magnetic viscosity is effective at inner most region (Fig. 11 and Fig. 12) and multi-dimensional outflow (Fig. 1) carries angular momentum outward. Thus amplification of magnetic fields is important not only for launching a jet by magnetic pressure, but also for enhancing mass accretion rate and energy deposition rate through weak interactions. In our study, we assume the axisymmetry of the system to save CPU time. In this case, the field built up by the effect of magnetorotational instability (MRI) decays due to Cowling’s anti-dynamo theorem (Shercliff 1965). However, the plasma beta becomes lower than unity in the jet region (Fig. 14), which is embodied by the amplification of B_ϕ fields (Figs. 13 and 15). Thus we consider that B_ϕ field is not amplified by MRI effects, but by winding-up of poloidal fields due to differential rotation. The typical timescale of winding-up at the inner most region will be (see Figs. 3 and 10)

$$\tau_{\text{wind}} \sim 2\pi \frac{d \ln r}{d\Omega} \sim \frac{2\pi \ln 10}{10^4} \sim 1.45 \times 10^{-3} \text{ s}. \quad (18)$$

This timescale will correspond to the steep rising of energy of B_ϕ around $t = 0.1$ s in Figs. 13 and 15. After the steep growth, when the strength of B_ϕ becomes comparable to the poloidal component, the growth rate declines since B_ϕ grows by winding the ‘weak’ poloidal component (Takiwaki et al. 2004). The final time of the simulation is determined when the Alfvén speed reaches to the order of the speed of light. This is understood as follows: Alfvén crossing time in the θ -direction at the innermost region becomes $r\Delta\theta/v_A = 10^6 \times (\pi/60)/c = 1.74 \times 10^{-6}$ s. Since the total timestep is several times of 10^6 , the final time is estimated to be several time, which is consistent with our results. The Alfvén speed is estimated to be

$$v_A = \frac{B}{\sqrt{4\pi\rho}} \sim 2.82 \times 10^8 \left(\frac{B}{10^{15}\text{G}} \right) \left(\frac{10^{12}\text{g cm}^{-3}}{\rho} \right)^{1/2} \text{ cm s}^{-1} \quad (19)$$

$$\sim 2.82 \times 10^{10} \left(\frac{B}{10^{15}\text{G}} \right) \left(\frac{10^8\text{g cm}^{-3}}{\rho} \right)^{1/2} \text{ cm s}^{-1}, \quad (20)$$

which means that the final time is determined not by the time when the amplitude of B_ϕ reaches to 10^{15}G around the equatorial plane, but by the time when the amplitude of B_ϕ reaches to 10^{15}G at low density region, that is, around the polar region where the jet is launched.

As for B_r and B_θ fields, from Fig. 13, some instabilities seem to grow and saturate, which is similar to the behavior of MRI (Hawley & Balbus 1991; Balbus & Hawley 1998). At present, we consider that these instabilities are MRI modes with a wavelength of maximum growth mode unresolved. However, we can not conclude that these instabilities are really unresolved MRI modes. This is due to the reason as follows: The dispersion relation of the linear MRI modes is obtained analytically by assuming that the accretion disk is supported by rotation (that is, in Kepler motion). On the other hand, as shown in Figs. 3 and 10, the radial velocity is non-zero in the accretion disks in this study. Moreover, the radial flow speed is super-slow magnetosonic (the speed of slow magnetosonic wave is almost same with that of Alfvén wave in this study: Fig. 11). Since MRI is the instability of the slow-magnetosonic waves in a magnetized and differentially rotation plasma, the dispersion relation may be changed considerably for such a super-slow magnetosonic flow. However, there is no analytic solution for such a flow at present, so we use the dispersion relation of MRI for the discussion here.

Ignoring entropy gradients, the condition for the instability of the slow-magnetosonic waves in a magnetized, differentially rotation plasma is (Balbus & Hawley 1991)

$$\frac{d\Omega^2}{d\ln r} + (\mathbf{k} \cdot \mathbf{v}_A)^2 < 0, \quad (21)$$

where \mathbf{k} is the vector of the wave number. The wavelength of maximum growth of the linear instability is

$$\lambda_0 = \frac{2\pi v_A}{\Omega} \sim 1.77 \times 10^3 \left(\frac{10^4 \text{s}^{-1}}{\Omega} \right) \left(\frac{B}{10^{13} \text{G}} \right) \left(\frac{10^{12} \text{g cm}^{-3}}{\rho} \right)^{1/2} \text{cm}. \quad (22)$$

Since λ_0 is much smaller than the grid size of the inner most region ($\Delta r = 3 \times 10^5 \text{cm}$), the linear MRI mode of maximum growth is not resolved in this study (note that the amplitudes of B_r and B_θ are of the order of 10^{13}G and much smaller than B_ϕ ; see Fig. 11). However, MRI grows as long as Eq. (21) holds. Since the value of the first term of Eq. (21) at the inner most region is $\sim -10^8 / \ln 10 \sim -4.34 \times 10^7$, it is confirmed that inner most region is unstable for MRI mode with the wave length longer than $\sim 10^3 (B/10^{13}\text{G})(10^{12}\text{g cm}^{-3}/\rho)^{1/2}\text{cm}$. The characteristic growing timescale is (Balbus & Hawley 1998; Akiyama et al. 2003; Proga et al. 2003)

$$\tau_{\text{MRI}} \sim 2\pi \left| \frac{d\Omega^2}{d\ln r} \right|^{-1/2} \sim 6.74 \times 10^{-4} \text{ s}, \quad (23)$$

which is seen in model 9 (Fig. 13) and model 8 (Fig. 15). The saturation level of B_r seems to be slightly higher than that of B_θ , which is similar to the results of the local simulations of MRI (Sano et al. 2004). Also, as shown in Fig. 16, the growth rate of B_r and B_θ components depends on the grid resolution, while the growth rate of B_ϕ does not depend on the grid resolution. In fact, the growth rate becomes smaller for a coarse mesh case (Fig. 16(a)). This is similar to the picture that B_r and B_θ are amplified by MRI, while B_ϕ is amplified by winding effect. The saturation level of B_r and B_θ seems not to be sensitive to the grid resolution. As stated above, in order to prove firmly that B_r and B_θ are amplified by MRI-like instability, dispersion relation of linear growing modes for super-slow magnetosonic flow has to be obtained analytically and the dispersion relation has to be reproduced by numerical simulations with finer grid resolution, which is outscope of this study.

As shown in Fig. 11, the estimated viscosity parameter becomes larger than 10^{-3} at almost all region in $r \leq 4 \times 10^4$ cm. Since the angular velocity becomes larger than 10^3 for $r \leq 6 \times 10^6$ cm (Fig. 10), this viscosity becomes effective in a timescale of second, which is comparable to our simulations. Thus we think this viscosity drives high mass accretion rate in the models with magnetic fields. However, as stated in section 3.2, the angular momentum cannot be transferred to infinity along the radial direction. As shown in Fig. 11, the flow is super-Alfvénic except for the inner most region. Thus angular momentum cannot be conveyed outward by Alfvén wave in the radial direction. At present, we consider that the outflow (including the jet) in the polar direction in model 9 should bring the angular momentum from the inner most region (see Fig. 1 bottom). This picture is similar to CDAF (Narayan et al. 2001). We are planning to present further analysis of this feature in the forth-coming paper.

Since the plasma beta can be of the order of unity at the inner most region (Fig. 14) and B_ϕ dominates B_r and B_θ at the region ($r \leq 7 - 8 \times 10^7$ cm), we can understand that the magnetic pressure from B_r and B_θ is much smaller than the radiation pressure (from photons, electrons, and positrons) and degenerate pressure. Thus, the jet cannot be launched by the effects of B_r and B_θ only. The winding-up effect is necessary to amplify B_ϕ field so that the magnetic pressure becomes comparable to the radiation and degenerate pressure. We saw that MRI-like instability seems to occur from the beginning of the simulations (see model 8 in Fig. 15). However, since the saturation level is not so high, the amplified energy of magnetic fields for B_r and B_θ cannot be seen well at first (see model 9 in Fig. 13 and model 10 in Fig. 15). This is because at the early phase the steady accretion disk is not formed and released gravitational energy is not so much (see Fig. 2). In model 11 and model 12, the initial total energies of magnetic fields are so high that the effect of MRI-like instability cannot be seen (Fig. 15).

As stated above, the axisymmetry of the system is assumed in this study. So winding up effect only amplifies $m = 0$ mode of B_ϕ . Usually, it is pointed out that saturation level of the winding up effects becomes lower when three dimensional simulations are performed (Hawley et al. 1995). Thus B_ϕ may not be amplified as strong as 10^{15}G . Also, at the present study, the timescale for B_ϕ fields at the inner most region to be amplified to $\sim 10^{15}\text{G}$ depends on the initial amplitude of the magnetic fields (see Figs. 13 and 15). However, if three dimensional simulations are performed, instabilities due to MRI(-like) modes do not decay due to Cowling’s anti-dynamo theorem. Also, the MRI(-like) modes with wave vectors whose ϕ components are non-zero, which amplify B_ϕ are included (Masada et al. 2006). If such MRI(-like) modes that amplify B_ϕ are included, the dependence of the dynamics on the initial amplitude of the magnetic fields may be diluted. We have to perform three dimensional calculations to see what happens in more realistic situations.

As stated above, the timestep becomes so small when the Alfvén crossing time becomes so small. Since this calculation is Newtonian, the speed of light is not included in the basic equations for macro physics (Eq. (1)-Eq. (6)). In fact, we found that the Alfvén speed becomes larger than the speed of light at some points by a factor of two or so at the final stage of simulations. Thus it will be one of the solutions to overcome this problem is to develop the special relativistic MHD code, in which the Alfvén speed is, of course, solved to be smaller than the speed of light.

In this study, we considered the ideal MHD without dissipation (it is, of course, numerical viscosity is inevitably included due to finite gridding effects). When resistive heating is efficient, considerable amount of energy in magnetic fields will be transferred to thermal energy by ohmic-like dissipation and reconnection, which will change the dynamics of collapsars so much. The problem is, however, that the properties of resistivity of high density and high temperature matter with strong magnetic fields are highly uncertain (it is noted that artificial resistivity is included in Proga et al. (2003) in order to account of the dissipation in a controlled way instead of allowing numerical effects to dissipate magnetic fields in an uncontrolled manner (see also Stone and Pringle 2001)).

Finally, we discuss the total explosion energy and bulk Lorentz factor of the jet. From Table 2, we can see that there seems to be a tendency that the mass of the jet becomes heavier when the initial amplitude of the magnetic fields are stronger (model 10, model 11, and model 12), although this tendency is not monotonic (model 8 and model 9). This will reflect that the jet is launched earlier and the density is still higher for a case with stronger initial magnetic fields. There seems to be also tendency that the energy of the jet becomes also larger when the initial amplitude of the magnetic fields is set to be stronger, although this tendency is not also monotonic (model 8 and model 9). This tendency is not

so remarkable since the mass of the jet is heavier for a stronger magnetic field case and the mass should have some amount of kinetic, thermal, and magnetic field energies. As for the models 8 and 9, the information of initial condition might be lost considerably since it takes much time to launch jets. From these results, we can conclude that no GRB jet is realized even if strong magnetic fields is assumed. We consider that there will be a possibility that a GRB jet is realized if we can perform numerical simulations for much longer physical time (say, $\sim 10 - 100$ s). In such long timescale simulations, the energy of B_ϕ fields should be much more than 10^{50} erg (see Figs. 13 and 15). Also, the density in the jet may become lower along with time, because considerable mass will falls into the black hole along the polar axis. Thus the terminal bulk Lorentz factor may be enhanced at later phase. In order to achieve such a simulation, the special relativistic code will be helpful, as mentioned above.

4.3. Prospect for Nucleosynthesis

It is radioactive nuclei, ^{56}Ni and its daughter nuclei, ^{56}Co , that brighten the supernova remnant and determine its bolometric luminosity. ^{56}Ni is considered to be synthesized through explosive nucleosynthesis because its half-life is very short (5.9 days). Thus it is natural to consider that explosive nucleosynthesis occurs in a hypernova that is accompanied by a GRB. However, it is not clearly known where the explosive nucleosynthesis occurs (e.g. Fryer et al. 2006a, Fryer et al. 2006b).

Maeda et al. (2002) have done a numerical calculation of explosive nucleosynthesis launching a jet by depositing thermal and kinetic energy at the inner most region. They have shown that a mass of ^{56}Ni sufficient to explain the observation of hypernovae ($\sim 0.5M_\odot$) can be synthesized around the jet region. In their calculation, all the explosion energy was deposited initially. Thus Nagataki et al. (2006) investigated the dependence of explosive nucleosynthesis on the energy deposition rate. They have shown that sufficient mass of ^{56}Ni can be synthesized as long as all the explosion energy is deposited initially, while the synthesized mass of ^{56}Ni is insufficient if the explosion energy is deposited for 10 s (that is, the energy deposition rate is 10^{51} erg s^{-1}). This is because matter starts to move outward after the passage of the shock wave, and almost all of the matter moves away from the central engine before the injection of thermal energy ($= 10^{52}$ erg) is completed, so the amount of mass where complete burning to synthesize ^{56}Ni becomes little for such a long-duration explosion (see also Nagataki et al (2003)).

On the other hand, it is pointed out the possibility that a substantial amount of ^{56}Ni is produced in the accretion disk and a part of it is conveyed outward by the viscosity-driven wind by some authors (MacFadyen & Woosley 1999; Pruet et al. 2003). However, there is

much uncertainty how much ^{56}Ni is ejected from the accretion disk. This problem depends sensitively on the viscosity effects. Further investigation is required to estimate how much ^{56}Ni is ejected.

In this study, we have found that mass of ^{56}Ni in the accretion disk (see Fig. 4) at the final stage of simulations is of the order of $10^{-3}M_{\odot}$ ($M_{\text{Ni}}^{\text{tot}}$ in Table 3). Thus if considerable fraction of the synthesized ^{56}Ni is ejected without falling into the black hole, there will be a possibility to supply sufficient amount of ^{56}Ni required to explain the luminosity of a hypernova. However, in the present study, the ejected mass of ^{56}Ni was found to be only $10^{-11} - 10^{-6}M_{\odot}$ ($M_{\text{Ni}}^{\text{esc}}$ in Table 3). This is because the entropy per baryon in the jet is so high (Fig. 17) that the light elements such as n , p , and He dominate in the jet. Thus we could not show that sufficient mass of ^{56}Ni was ejected from the accretion disk in the present study. There will be two possibilities to extract enough amount of ^{56}Ni from the accretion disk. One is that ^{56}Ni might be extracted efficiently from the accretion disk at later phase. Since typical temperature of the accretion disk will be lower when the mass of the central black hole becomes larger, the entropy per baryon in the jet will be decreased (Nagataki et al. 2002). This feature should suggest that ^{56}Ni dominates in the jet component at the late phase. The other one is that some kinds of viscosities might work to convey the matter in the accretion disk outward efficiently. In MacFadyen and Woosley (1999), they included α -viscosity and showed that considerable amount can be conveyed. Since α viscosity is not included in this study, such a feature was not seen. However, when three dimensional simulations with higher resolution than in this study are done, much more modes of magnetic fields should be resolved, and some of them might be responsible for viscosities and work like α -viscosity.

We discuss the possibility to synthesize heavy elements in collapsars. We have shown that neutron-rich matter with high entropy per baryon is ejected along the jet axis (Figs. 17 and 18). This is because electron capture dominates positron capture in the accretion disk (Fig. 6). Thus there is a possibility that r -process nucleosynthesis occurs in the jet (Nagataki et al. 1997; Nagataki 2000; Nagataki 2001; Nagataki & Kohri 2001; Wanajo et al. 2002; Suzuki & Nagataki 2005; Fujimoto et al. 2006). Moreover, we found that mass element with high Y_e (~ 0.522) appears around the polar axis near the black hole. This is because ν_e capture dominates $\bar{\nu}_e$ capture at the region. This is because flux of ν_e from the accretion disk (note that ν_e comes from electron capture) is sufficiently large to enhance Y_e at the region. In such a high Y_e region, there will be a possibility that r/p -process nucleosynthesis occurs (Wanajo 2006). We are planning to perform such a numerical simulations in the very near future. Also, there is a possibility that much neutrons are ejected from the jet since the entropy per baryon amounts to the order of 10^4 . If so, there may be a possibility that signals from the neutron decays may be observed as the delayed bump of the light curve of the afterglow (Kulkarni 2005) or gamma-rays (Razzaque & Mészáros 2006a). Also, GeV

emission may be observed by proton-neutron inelastic scattering (Mészáros & Rees 2000; Rossi et al. 2006; Razzaque & Mészáros 2006b). Finally, note that a careful treatment of neutrino transfer is important for the r- and r/p-process nucleosynthesis. As stated in section 4.1, the optically thin limit may break down at the high density region. When the matter becomes to be opaque to neutrinos, the neutrinos become to be trapped and degenerate. In the high density limit, the chemical equilibrium is achieved as $\mu_e + \mu_p = \mu_n + \mu_{\nu_e}$ where μ_e , μ_p , μ_n , and μ_{ν_e} are chemical potentials of electrons, protons, neutrons, and electron-type neutrinos. When the chemical potential of electron-type neutrinos is not negligible, the electron capture does not proceed further and electron fraction does not decrease so much (Sato 1975), which should be crucial to the r- and r/p-process nucleosynthesis.

4.4. General Relativistic Effects

In this section, we discuss general relativistic effects that we are planning to include in our magnetohydrodynamic simulation code.

First, we still believe that effects of energy deposition due to weak interactions (especially, neutrino anti-neutrino pair annihilation) can be a key process as the central engine of GRBs. In fact, the temperature of the accretion disk becomes higher especially for a Kerr black hole since the gravitational potential becomes deeper and much gravitational energy is released at the inner most region and the radius of the inner most stable orbit becomes smaller for a Kerr black hole (Popham et al. 1999; MacFadyen & Woosley 1999). This effect will enhance the luminosity of the neutrinos from the accretion disk (Popham et al. 1999), and the neutrino pair annihilation (Asano & Fukuyama 2000; Miller et al. 2003; Kneller et al. 2006; Gu et al. 2006). In the vicinity of the black hole, most of neutrinos and anti-neutrinos come shadows due to the bending effects of the neutrino geodesics. Since the shape and position of the black hole shadow depend on the physical parameters of the black hole (Bardeen 1973; Takahashi 2004, 2005), the effective area emitting the most of the neutrino flux just outside of the black hole shadows is also determined by the black hole parameters. These effects are included only when geodesics and disk structures are precisely calculated.

Since according to our simulations the plasma beta ($= p_{\text{gas}} + p_{\text{radiation}} / p_{\text{mag}}$) in the polar region is lower than the plasma beta in other regions and the minimum values of the plasma beta is 0.193. This means that the polar region is magnetically dominated. In such regions where the magnetic energy is dominated such as a force-free field, the extraction of the rotational energy of the black hole is expected as Poynting flux (Blandford & Znajek 1977) and the negative energy (Blandford & Payne 1982; Takahashi et al. 1990). Although these

effects have been confirmed numerically by many authors (Koide 2003; Mizuno et al. 2004b; Komissarov 2005; Hawley & Krolic 2006; McKinney 2006), there are many unsolved issues on the central engine of GRBs. Especially, the neutrino radiation from the negative energy fluid in the realistic general relativistic accretion flow is one of the unsolved issue. The past studies roughly estimate the extraction energy due to the Blandford-Znajek process to become non-negligible amount to the explosion of the long GRBs (e.g. Lee et al. 2000a, 2000b; Di Matteo et al. 2002).

4.5. Variety of Initial Conditions

The properties of a progenitor of GRBs are still unknown. There are much uncertainties on mass loss rate, final mass, angular momentum distribution, amplitude and configuration of magnetic fields prior to collapse. These properties will depend not only on initial mass and metallicity of progenitors but also on the presence (or absence) and properties of companion stars (Maeder & Meynet 2001; Woosley & Heger 2006; MacFadyen et al. 2005). Thus it is necessary to perform numerical simulations with many models of progenitors to ensure the validity of the mechanism to launch a GRB jet from progenitors. In particular, we consider that the initial angular momentum distribution should be important since the mass accretion rate depends on it very sensitively.

4.6. Prospects for Improvements of Numerical Scheme

As shown in Eq. (22), the critical wavelength of maximum growth of the linear MRI instability is quite short, so adaptive mesh refinement method (e.g. Norman 2005; Zhang and MacFadyen 2006; Morsony et al. 2006) is inevitably required to resolve the critical wavelength in a collapsar. Of course, much CPU time is required to perform three dimensional calculation with adaptive mesh refinement method. Moreover, when we try to include neutrino transfer code, three dimensions are required additionally for the momentum space. However, people will be able to realize such an expensive simulation in the near future with a help of rapidly growing power of super-computers. Of course, we are planning to devote ourselves to developing such a numerical code.

5. SUMMARY AND CONCLUSION

We have performed two-dimensional magnetohydrodynamic simulations by the ZEUS-2D code to investigate the dynamics of a collapsar that generates a GRB jet, taking account of realistic equation of state (contribution of electrons, positrons, radiation, and ideal gas of nuclei), neutrino cooling and heating processes, magnetic fields, and gravitational force from the central black hole and self gravity.

We have found that neutrino heating processes (neutrino and anti-neutrino pair annihilation, and ν_e and $\bar{\nu}_e$ captures on free nucleons) are not so efficient to launch a jet. We have found that a jet is launched by magnetic fields (in particular, B_ϕ fields that are amplified by the winding-up effect). However, the ratio of total energy relative to the rest mass energy in the jet at the final stage of simulations suggests that the bulk Lorentz factor of the jet will not reach to as high as several hundred, so we conclude the jet seen in this study will not be a GRB jet. We also found that the mass accretion rate seems to be enhanced in the models with magnetic fields. This might be because angular momentum is efficiently transferred by the viscosity due to the magnetic fields and multi-dimensional flow.

Since GRB jets are not obtained in this study, we consider that general relativistic effects, by which the efficiency of energy deposition through weak interactions will be enhanced and rotation energy of the black hole will be transferred to matter through the magnetic fields, will be important to generate a GRB jet. Thus we are planning to develop a general relativistic magnetohydrodynamics code in the very near future. Also, the accretion disk with magnetic fields may still play an important role to launch a GRB jet, and it may be seen if we can perform numerical simulations for much longer physical time (say, $\sim 10 - 100$ s). To realize such a simulation, the special relativistic code will be helpful because the Alfvén velocity is limited to the speed of light.

We have shown that considerable amount of ^{56}Ni is synthesized in the accretion disk. Thus if some fraction of the synthesized ^{56}Ni is ejected without falling into the black hole, there will be a possibility for the accretion disk to supply sufficient amount of ^{56}Ni required to explain the luminosity of a hypernova. Also, we have shown that neutron-rich matter with high entropy per baryon is ejected along the rotation axis. This is because electron capture dominates positron capture. Moreover, we found that the electron fraction becomes larger than 0.5 around the polar axis near the black hole. This is because ν_e capture dominates $\bar{\nu}_e$ capture at the region. Thus there will be a possibility that r -process and r/p -process nucleosynthesis occur at these regions. Finally, much neutrons will be ejected from the jet, which suggests that signals from the neutron decays may be observed as the delayed bump of the light curve of the afterglow or gamma-rays.

S.N. is grateful to S. Akiyama, R. Blandford, S. Fujimoto, S. Inutsuka, S. Mineshige, T. Sano, S. Yamada, T. Yamasaki and M. Watanabe for useful discussion. The computation was carried out on NEC SX-5 and SX-8, SGI Altix3700 BX2, and Compaq Alpha Server ES40 at Yukawa Institute for Theoretical Physics, Kyoto University. This work is in part supported by a Grant-in-Aid for the 21st Century COE “Center for Diversity and Universality in Physics” from the Ministry of Education, Culture, Sports, Science and Technology of Japan. S.N. is partially supported by Grants-in-Aid for Scientific Research from the Ministry of Education, Culture, Sports, Science and Technology of Japan through No. 16740134. R.T. is partially supported by Japan Society for the Promotion of Science No. 1710519. T.T is partially supported by Japan Society for the Promotion of Science.

REFERENCES

- Akiyama, S., et al. 2003, ApJ, 584, 954
- Aloy, M.A., et al. 2000, ApJ, 531, L119
- Asano, K., Fukuyama, T. 2000, ApJ, 531, 949
- Balbus, S.A., Hawley, J.F. 1991, ApJ, 376, 214
- Balbus, S.A., Hawley, J.F. 1998, Rev. Mod. Phys., 70, 1
- Bardeen, J.M., 1973, in Black Holes, ed. C. DeWitt and B. DeWitt (Gordon and Breach, New York)
- Bethe, H.A. 1990, Rev. Mod. Phys., 62, 801
- Blandford, R.D., Znajek, R.L. 1977, MNRAS, 179, 433
- Blandford, R.D., Payne, D.G. 1982, MNRAS, 199, 883
- Blinnikov, S.I., Dunina-Barkovskaya, N.V., Nadyozhin, D.K. 1996, ApJ, 106, 171
- Bloom, J.S., et al. 1999, Nature, 401, 453
- Bloom, J.S., Kulkarni, S.R., Djorgovski, S.G. 2002, AJ, 123, 1111
- Buras, R., et al. 2006, A&A, 447, 1049
- Chen, W.-X., Beloborodov, A.M. 2006, ApJ, accepted (astro-ph/0607145)
- Cooperstein, J., van den Horn, L.J., Baron, E.A. 1986, ApJ, 309, 653

- Di Matteo, T., Perna, R., Narayan, R. 2002, ApJ, 579, 706
- Fryer, C., Mészáros, P. 2000, ApJ, 588, L25
- Fryer, C.L., et al. 2006, ApJ, 646, L131
- Fryer, C.L., Young, P.A., Hungerford, A.L. 2006, astro-ph/0604471
- Fujimoto, S., et al. 2006, ApJ, 644, 1040
- Galama, T.J., et al. 1998, Nature, 395, 670
- Galama, T.J., et al. 2000, ApJ, 536, 185
- Garnavich, P.M., et al. 2003, ApJ, 582, 924
- Goodman, J., Dar, A., Nussinov, S. 1987, ApJ, 314, L7
- Gorosabel, J. et al. 2003, A&A, 409, 123
- Gu, W.-M., Liu, T., Lu, Ju-Fu, 2006, ApJL, 643, 87
- Hawley, J.F., Balbus, S.A. 1991, ApJ, 376, 223
- Hawley, J.F., Gammie, C.F., Balbus, S.A. 1995, ApJ, 440, 742
- Hawley, J.F., Krolik, J.H. 2006, ApJ, 641, 103
- Heger, A., Langer, N., Woosley, S.E. 2000, ApJ, 528, 368
- Herant, M.E., Benz, W., Colgate, S.A. 1992, ApJ, 395, 642
- Herant, M.E., et al. 1994, ApJ, 435, 339
- Hjorth, J., et al. 2003, Nature, 423, 847
- Igumenshchev, I.V., Abramowicz, M.A. 2000, ApJS, 130, 463
- Itoh, N., et al. 1989, ApJ, 339, 354
- Iwamoto, K., et al., 1998, Nature, 395, 672
- Kneller, J.P., McLaughlin, G.C., Surman, R.A. 2006, JPhG, 32, 443
- Koide, S. 2003, Phys. Rev. D., 67, 104010
- Komissarov, S.S. 2005, MNRAS, 359, 801

- Kotake, K., et al. 2003, ApJ, 595, 304
- Kulkarni, S.R. 2005 (astro-ph/0510256)
- Lee, H. K., Wijers, R. A. M. J., Brown, G. E., 2000, Physics Reports, 325, 83
- Lee, H. K., Brown, G. E., Wijers, R. A. M. J., 2000, ApJ, 536, 416
- Lee, W.H., Ramirez-Ruiz, E. 2006, ApJ, 641, 961
- MacFadyen, A.I., Woosley, S.E., ApJ, 1999, 524, 262
- MacFadyen, A.I., Ramires-Ruiz, E., Zhang, W. 2005, astro-ph/0510192
- Maeda, K., et al., 2002, ApJ, 565, 405
- Maeder, A., Meynet, G. 2001, A&A, 373, 555
- Masada, Y., Sano, T., Takabe, H. 2006, ApJ, 641, 447
- Mazzali, P.A., et al. 2006, astro-ph/0603567
- McKinney, J.C. 2006, MNRAS, accepted (astro-ph/0603045)
- Mestel, L., Spruit, H.C. 1967, MNRAS, 226, 57
- Mészáros, P., Rees, M. 2000, ApJ, 541, L5
- Miller, W. A., George, N. D., Kheyeets, A., McGhee, J. M., 2003, ApJ, 583, 833
- Mirabal, N., et al. 2006, ApJ, 643, L99
- Mizuno, Y. et al. 2004a, ApJ, 606, 395
- Mizuno, Y. et al. 2004b, ApJ, 615, 389
- Morsony, B.J., Lazzati, D., Begelman, M.C. 2006, astro-ph/0609254
- Nagataki, S., Hashimoto, M., Sato, K., Yamada, S. 1997, ApJ, 486, 1026
- Nagataki, S., 2000, ApJS, 127, 141
- Nagataki, S. 2001, ApJ, 551, 429
- Nagataki, S., Kohri, K. 2001, PASJ, 53, 547
- Nagataki, S. et al. 2002, Aph, 18, 551

- Nagataki, S., et al. 2003, ApJ, 596, 401
- Nagataki, S., Mizuta, A., Sato, K. 2003, ApJ, accepted (astro-ph/0601111).
- Narayan, R., Piran, T., Kumar, P. 2001, ApJ, 557, 949
- Nishimura, S., et al. 2006, ApJ, 642, 410
- Norman, M.L. 2005, in Adaptive Mesh Refinement: Theory and Applications, ed. T. Plewa, T. Linde, V.G. Weirs (Berlin: Springer)
- Paczynski, B., Witta, P.J. 1980, A&A, 88, 23
- Popham, R., Woosley, S.E., Fryer, C. 1999, ApJ, 518, 356
- Price, P.A., et al. 2003, Nature, 423, 843
- Proga, D., MacFadyen, A.I., Armitage, P.J., Begelman, M.C. 2003, ApJ, 599, L5
- Proga, D., Begelman, M.C. 2003, ApJ, 582, 69
- Proga, D. 2005, ApJ, 629, 397
- Pruet, J., Woosley, S.E., Hoffman, R.D. 2003, ApJ, 586, 1254
- Razzaque, S., Mészáros, P. 2006, JCAP, 0606 006
- Razzaque, S., Mészáros, P. 2006, astro-ph/0601652
- Reichart, D.E. 1999, ApJ, 521, L111
- Rockefeller, G., Fryer, C.L., Li, H. 2006, astro-ph/0608028
- Rossi, E.M., Beloborodov, A.M., Rees, M.J. 2006, MNRAS, 369, 1797
- Rosswog, S., Liebendörfer 2003, MNRAS, 342, 673
- Rybicki, G. B., Lightman, A. P., 1979, Radiative Process in Astrophysics (New York: John Wiley & Sons)
- Sano, T., Inutsuka, S., Turner, N.J., Stone, J.M. 2004, ApJ, 605, 321
- Sato, K. 1975, PThPh, 54, 1325
- Sekiguchi, Y., Shibata, M. 2005, Phys. Rev. D, 71, 084013
- Shercliff, J.A. 1965, A textbook of magnetohydrodynamics (Pergamon, Oxford)

- Shibata, M., Sekiguchi, Y. 2005, *Phys. Rev. D*, 71, 024014
- Stanek, E.Z. 2003, *ApJ*, 591, L17
- Stone, J.M., Norman, M.L. 1992a, *ApJS*, 80, 753
- Stone, J.M., Norman, M.L. 1992b, *ApJS*, 80, 791
- Stone, J.M., Pringle, J.E. 2001, *MNRAS*, 322, 461
- Suzuki, T.K., Nagataki, S. 2005, *ApJ*, 628, 914
- Takahashi, K., El Eid, M.F., Hillebrandt, W. 1978, *A&A*, 67, 185
- Takahashi, M., Nitta, S., Tatematsu, Y., & Tomimatsu, A. 1990, *ApJ*, 363, 206
- Takahashi, R., 2004, *ApJ*, 611, 996
- Takahashi, R., 2005, *PASJ*, 57, 273
- Takiwaki, T., et al. 2004, *ApJ*, 616, 1086
- Thielemann, F.-K., Nomoto, K., Hashimoto, M. 1996, 460, 408
- Vreeswijk, P.M., 2001, *A&A*, 380, L21
- Wanajo, S., Itoh, N., Ishimaru, Y., Nozawa, S., Beers, T.C. 2002, *ApJ*, 577, 853
- Wanajo, S. 2006, *astro-ph/0602488*
- Weber, E.J., Davis, L. 1967, *ApJ*, 148, 217
- Woosley, S.E., 1986, in *Nucleosynthesis and Chemical Evolutions*, eds. B. Hauck, A. Maeder, G. Meynet (Geneva: Geneva Observatory), 1
- Woosley, S.E., *ApJ*, 1993, 405, 273
- Woosley, S.E., Eastman, R.G., Schmidt, B.P. 1999, *ApJ*, 516, 788
- Woosley, S.E., Heger, A. 2006, *ApJ*, 637, 914
- Zhang, W., MacFadyen, A.I. 2006, *ApJS*, 164, 255

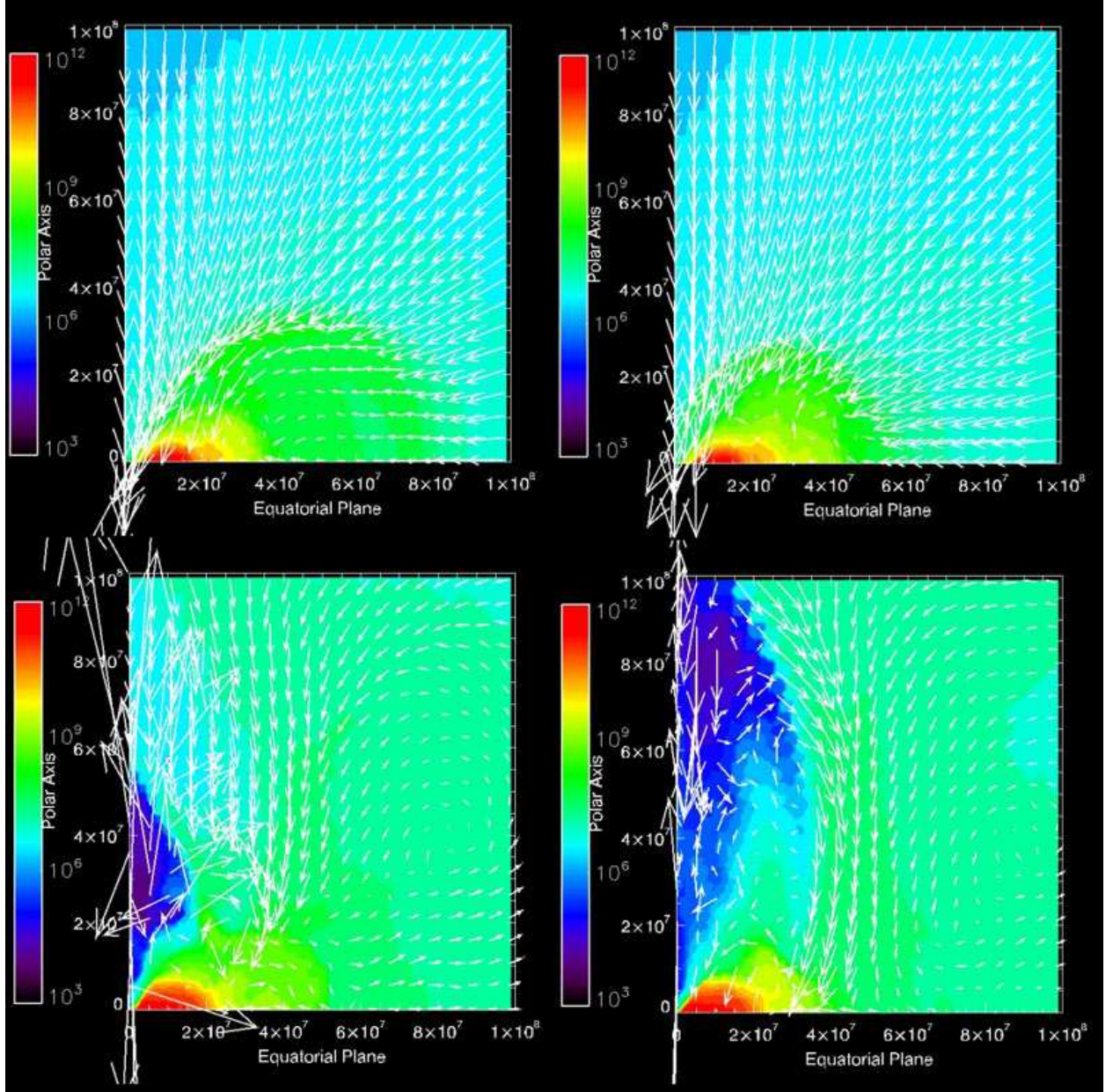


Fig. 1.— Top panels: density contour with velocity fields for model 0 at $t = 2.1$ s (left panel) and $t = 2.2$ s (right panel). Bottom panels: same with upper panels, but for model 9. The color represents the density (g cm^{-3}) in logarithmic scale ($10^3 - 10^{12}$). In this figure, the central region of the progenitor ($r \leq 10^8 \text{ cm}$) is shown. Vertical axis and horizontal axis represent rotation axis and equatorial plane, respectively.

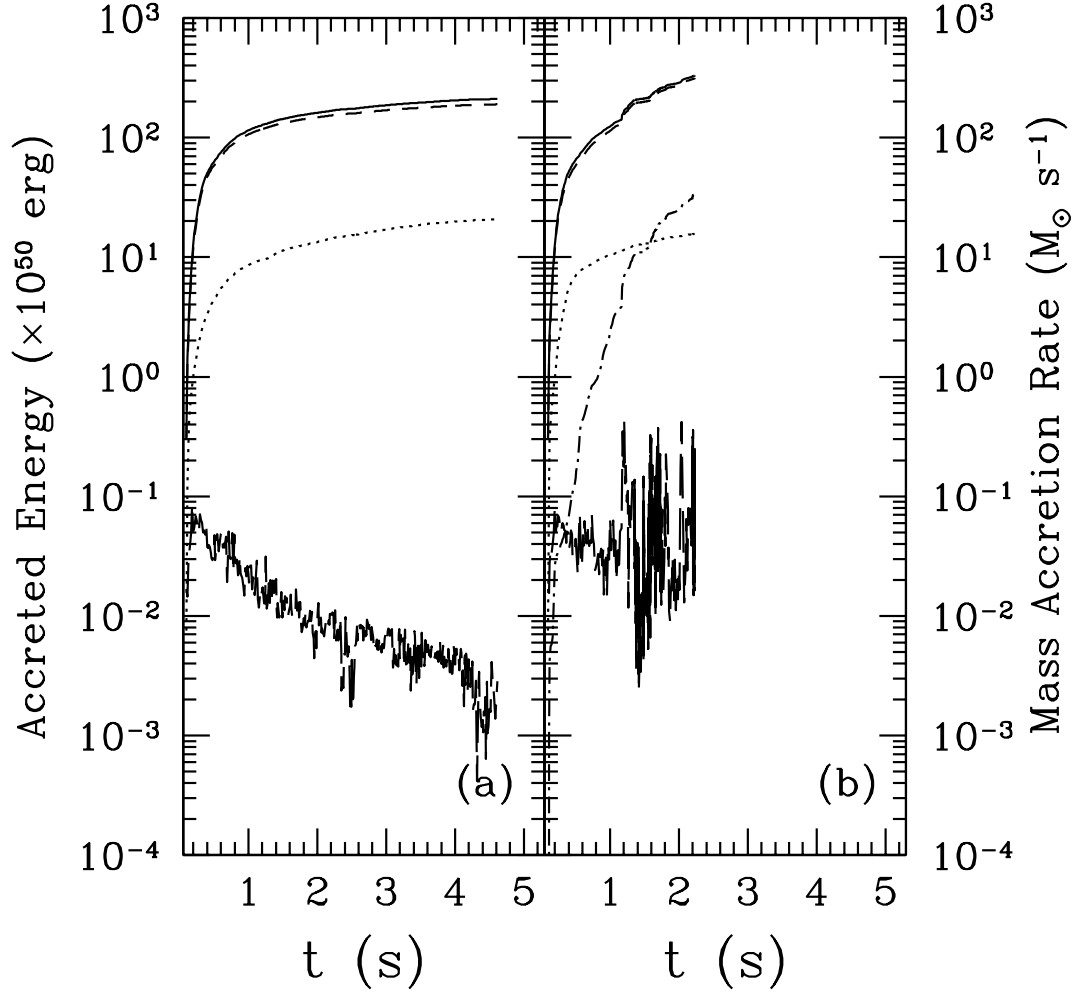


Fig. 2.— Solid, short-dashed, dotted, dot-dashed lines represent accreted total energy, kinetic energy, thermal energy, and electro-magnetic energy ($\times 10^{50}$ erg) into the black hole as a function of time, respectively. Long-dashed lines represent the mass accretion rate ($M_{\odot} \text{ s}^{-1}$) as a function of time. Left panel shows the case for model 0, while right panel represents the case for model 9. Note that in the case of model 0, the electro-magnetic energy is set to be zero.

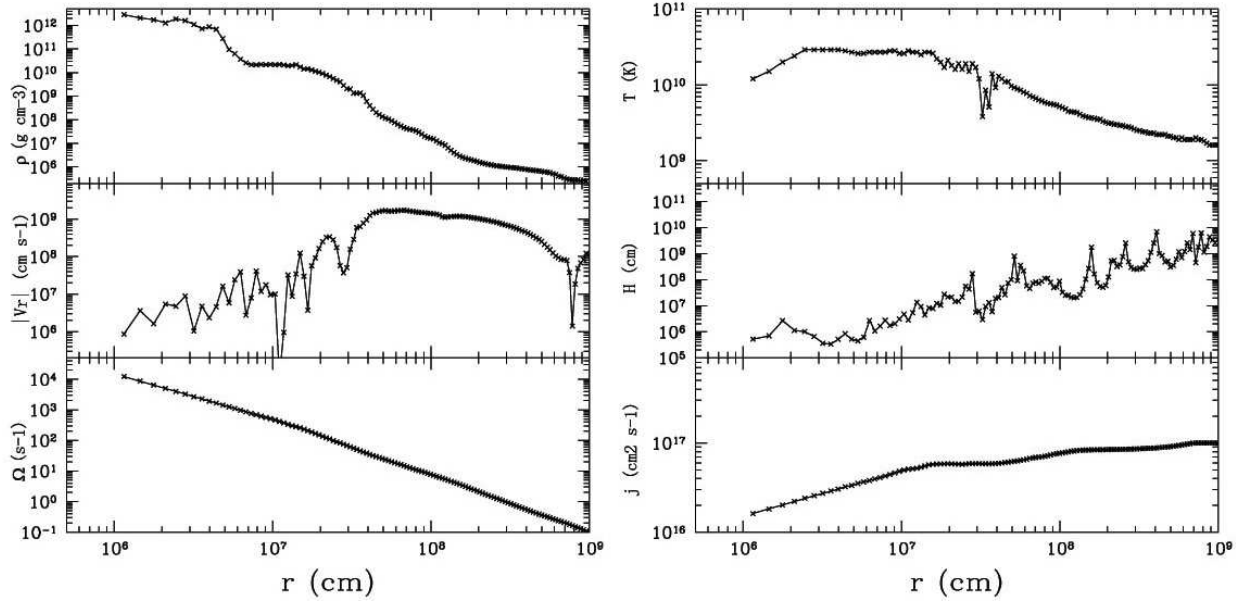


Fig. 3.— Profiles of density, absolute value of radial velocity, angular frequency, temperature, density scale height, and specific angular momentum at the equatorial plane for model 0 at $t = 2.2$ s.

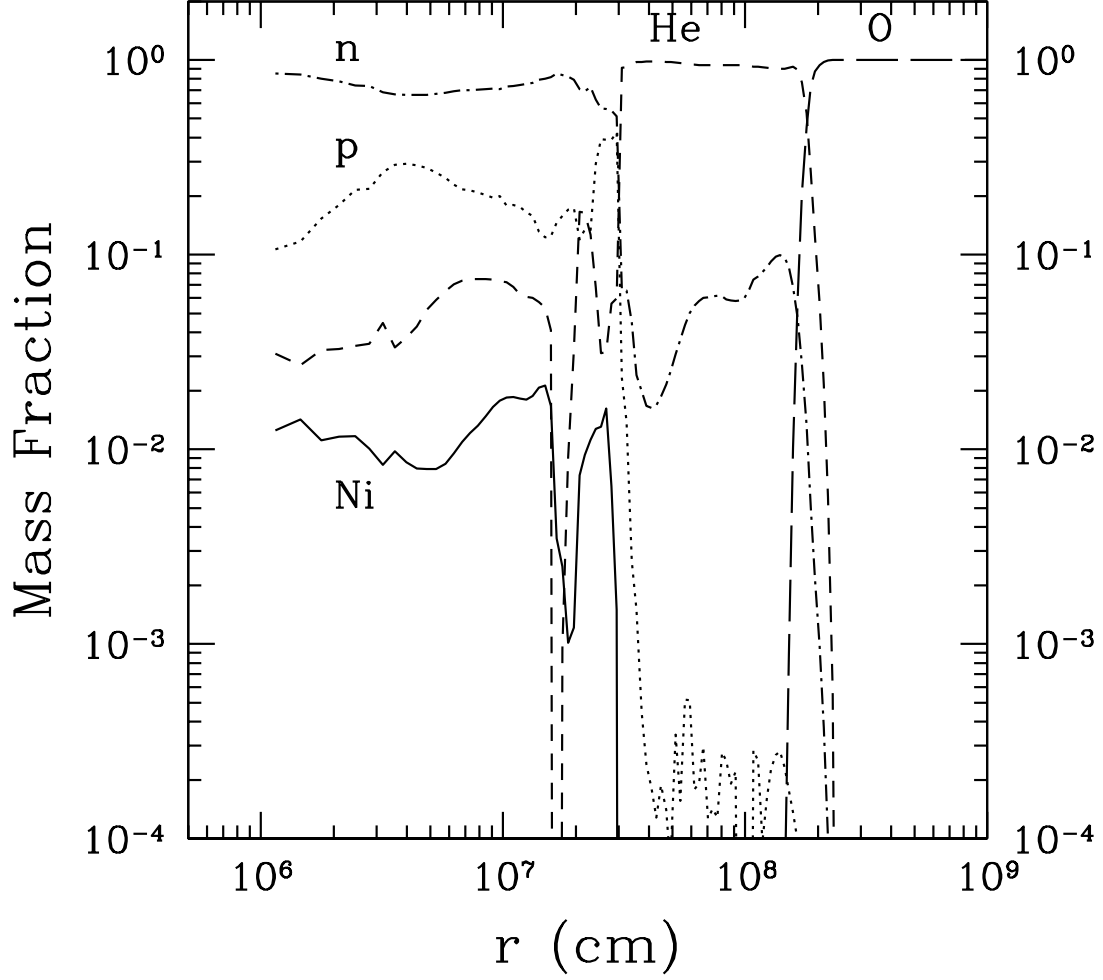


Fig. 4.— Profiles of mass fraction for nuclear elements at the equatorial plane for model 0 at $t = 2.2$ s. Dot-dashed, dotted, short-dashed, long-dashed, and solid lines represent mass fraction of n , p , ${}^4\text{He}$, ${}^{16}\text{O}$, and ${}^{56}\text{Ni}$, respectively.

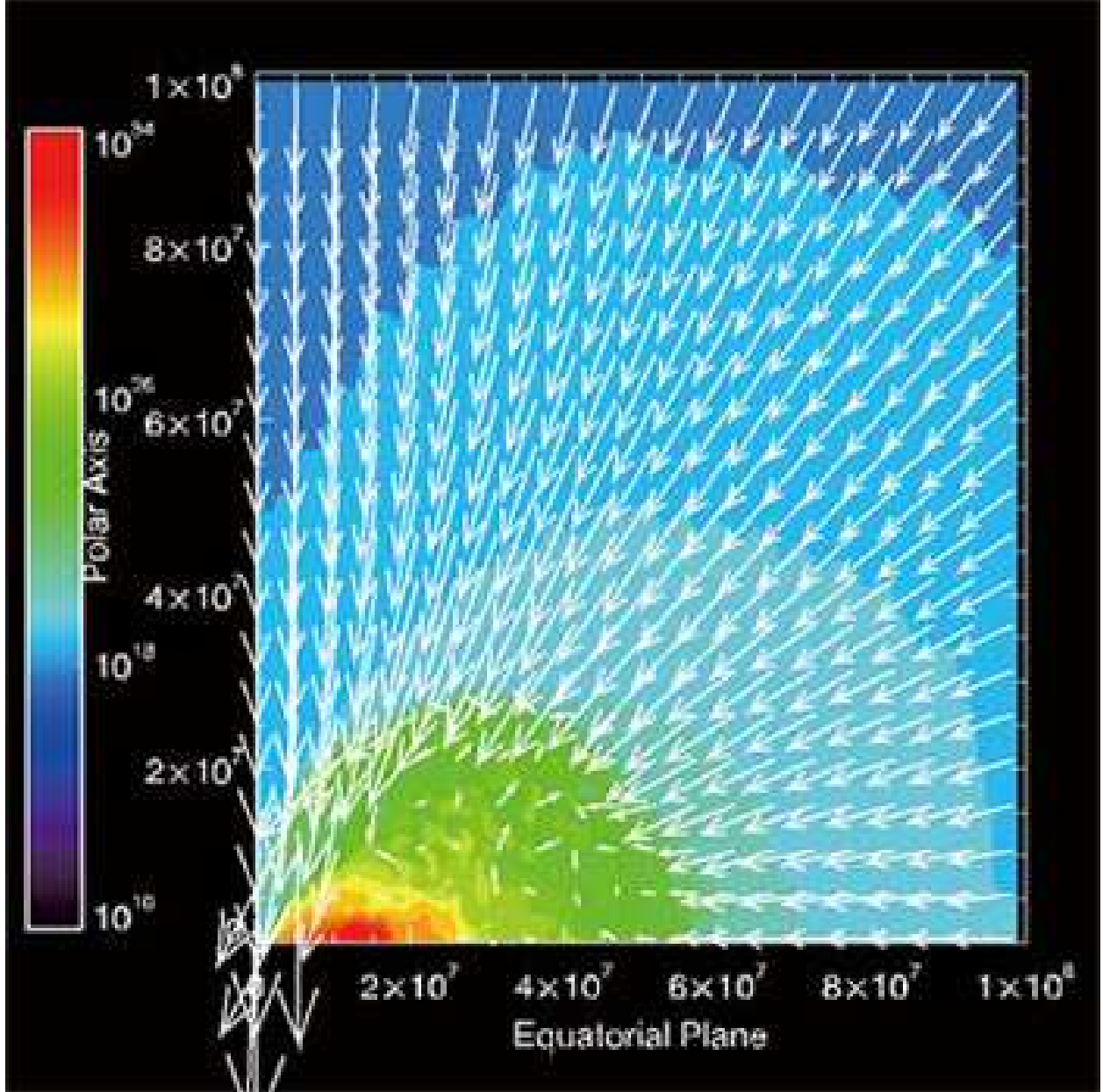


Fig. 5.— Contour of neutrino cooling rate with velocity fields for model 0 at $t = 2.2$ s. The color represents the emissivity of neutrinos ($\text{erg cm}^{-3} \text{s}^{-1}$) in logarithmic scale ($10^{10} - 10^{34}$).

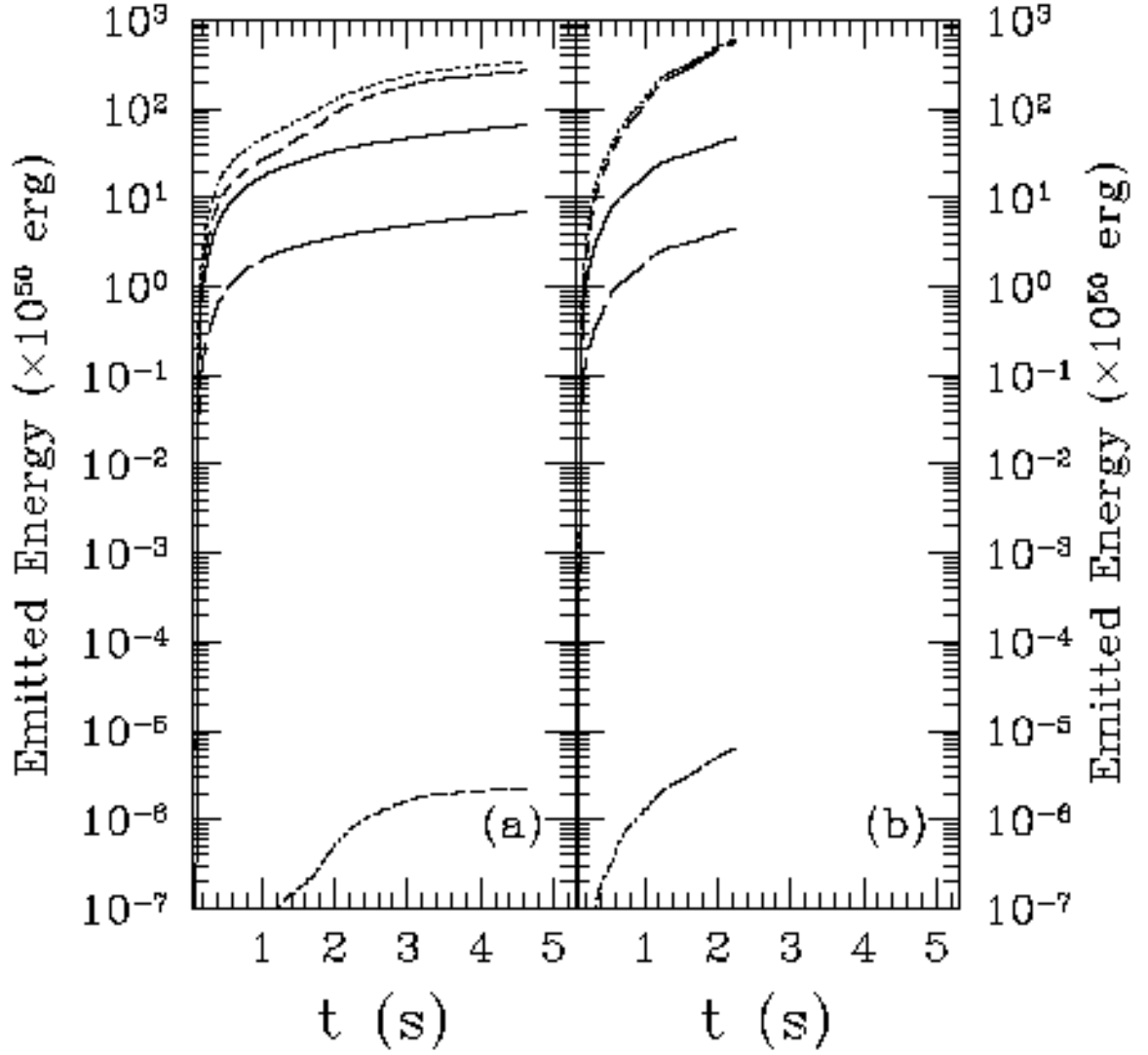


Fig. 6.— Cumulative energy ($\times 10^{50}$ erg) of emitted neutrinos for each process as a function of time. Dot-dashed, long-dashed, solid, short-dashed, and dotted lines represent plasmon decay, electron-positron pair annihilation, positron capture, electron capture, and summation of all processes. Left panel shows the case for model 0, while right panel shows model 9.

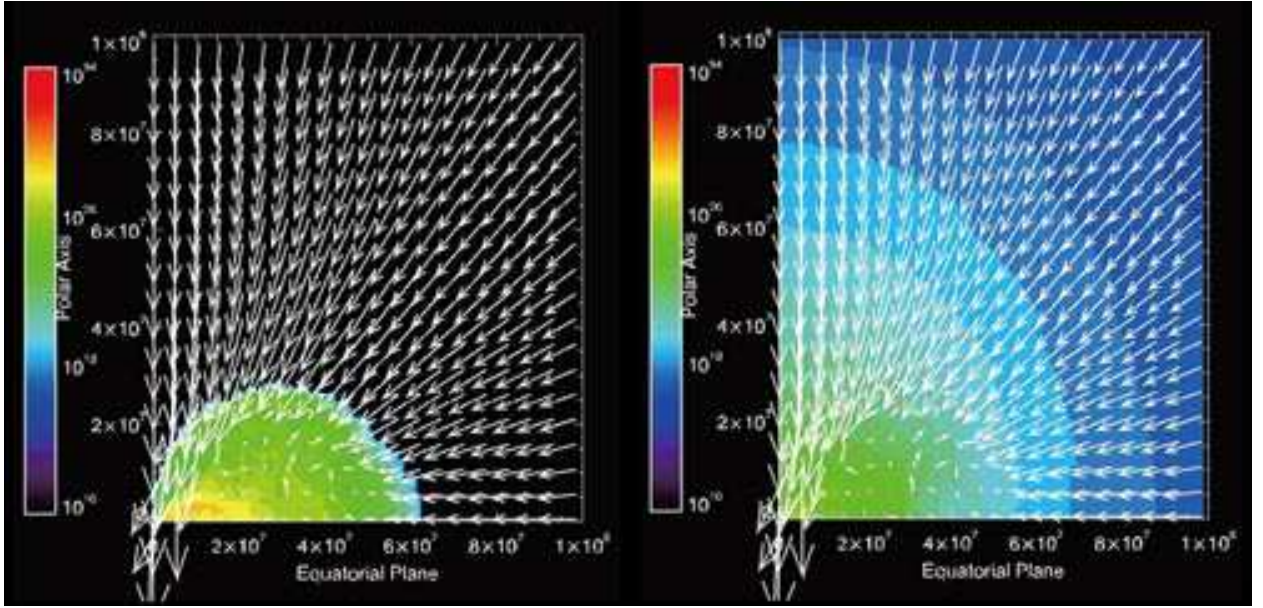


Fig. 7.— Contour of neutrino heating rate with velocity fields for model 0 at $t = 2.2$ s. The color represents the energy deposition rate ($\text{erg cm}^{-3} \text{s}^{-1}$) in logarithmic scale ($10^{10} - 10^{34}$). Left panel shows the energy deposition rate due to ν_e and $\bar{\nu}_e$ captures on free nucleons, while right panel shows the energy deposition rate due to ν and $\bar{\nu}$ pair annihilations (three flavors are taken into account).

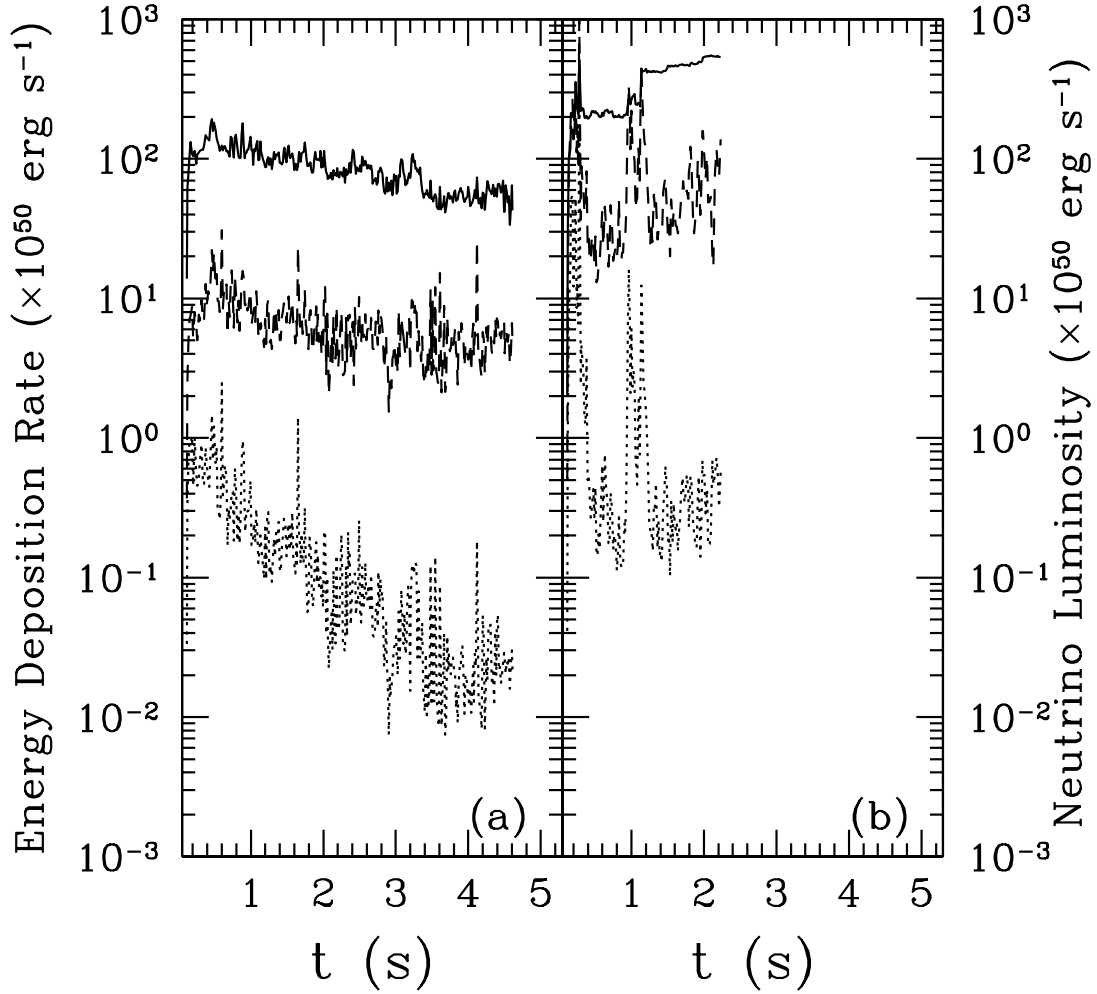


Fig. 8.— Neutrino luminosity (solid lines), energy deposition rate due to ν and $\bar{\nu}$ pair annihilations (dotted lines), and energy deposition rate due to ν_e and $\bar{\nu}_e$ captures on free nucleons (dashed line) as a function of time. The unit is $10^{50} \text{ erg s}^{-1}$. Left panel shows the case for model 0, while right panel shows the case for model 9.

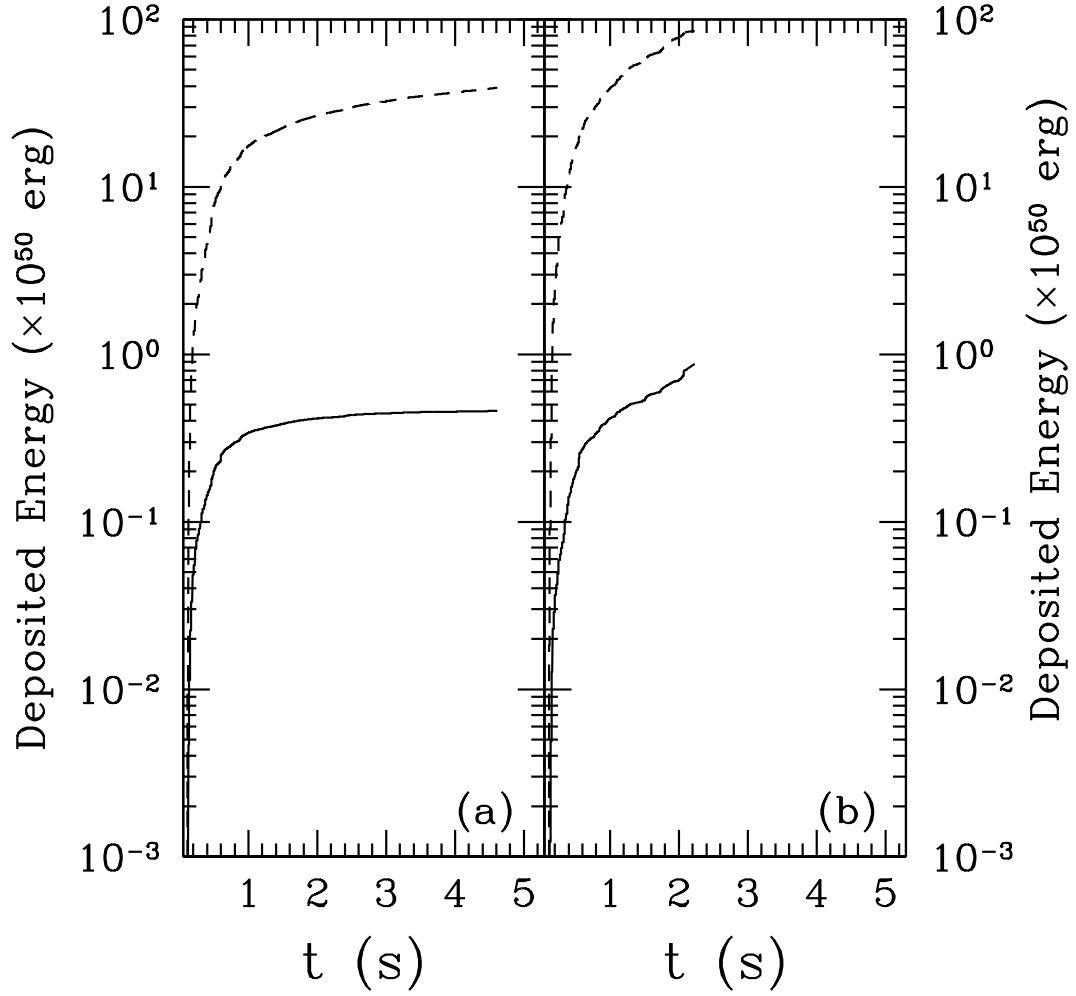


Fig. 9.— Integrated deposited energy ($\times 10^{50}$ erg) due to ν and $\bar{\nu}$ pair annihilations (solid lines) and ν_e and $\bar{\nu}_e$ captures on free nucleons (dashed lines) as a function of time. Left panel shows the case for model 0, while right panel shows the case for model 9.

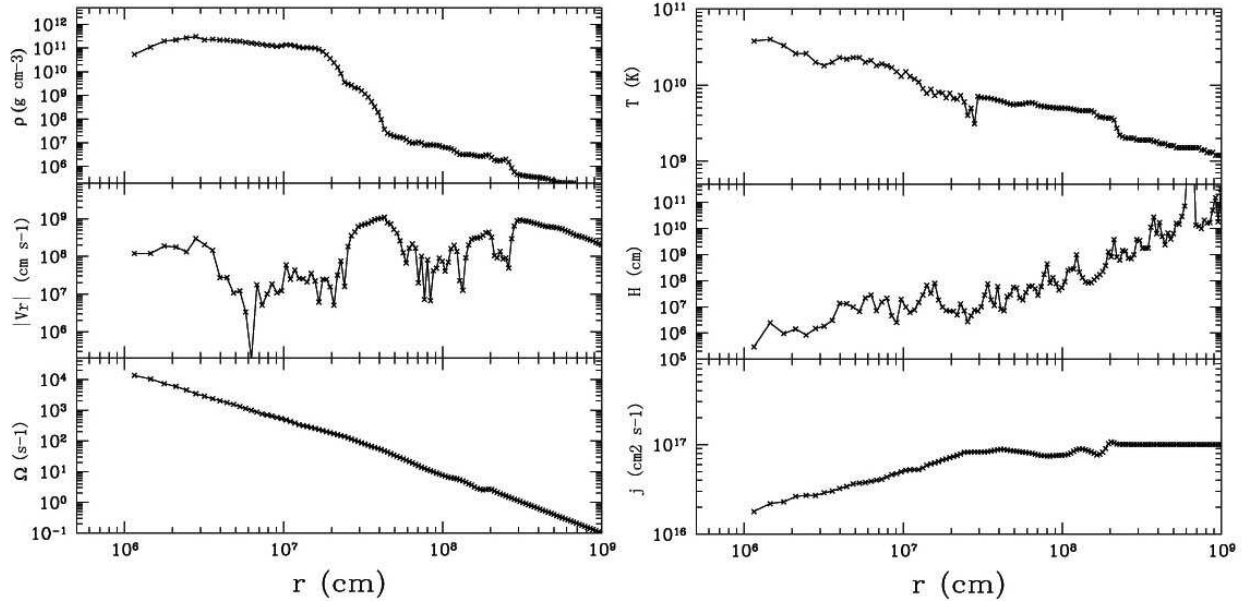


Fig. 10.— Same with Fig.3, but for model 9. Note that the radial velocity profile is not similar to model 0 at small radius.

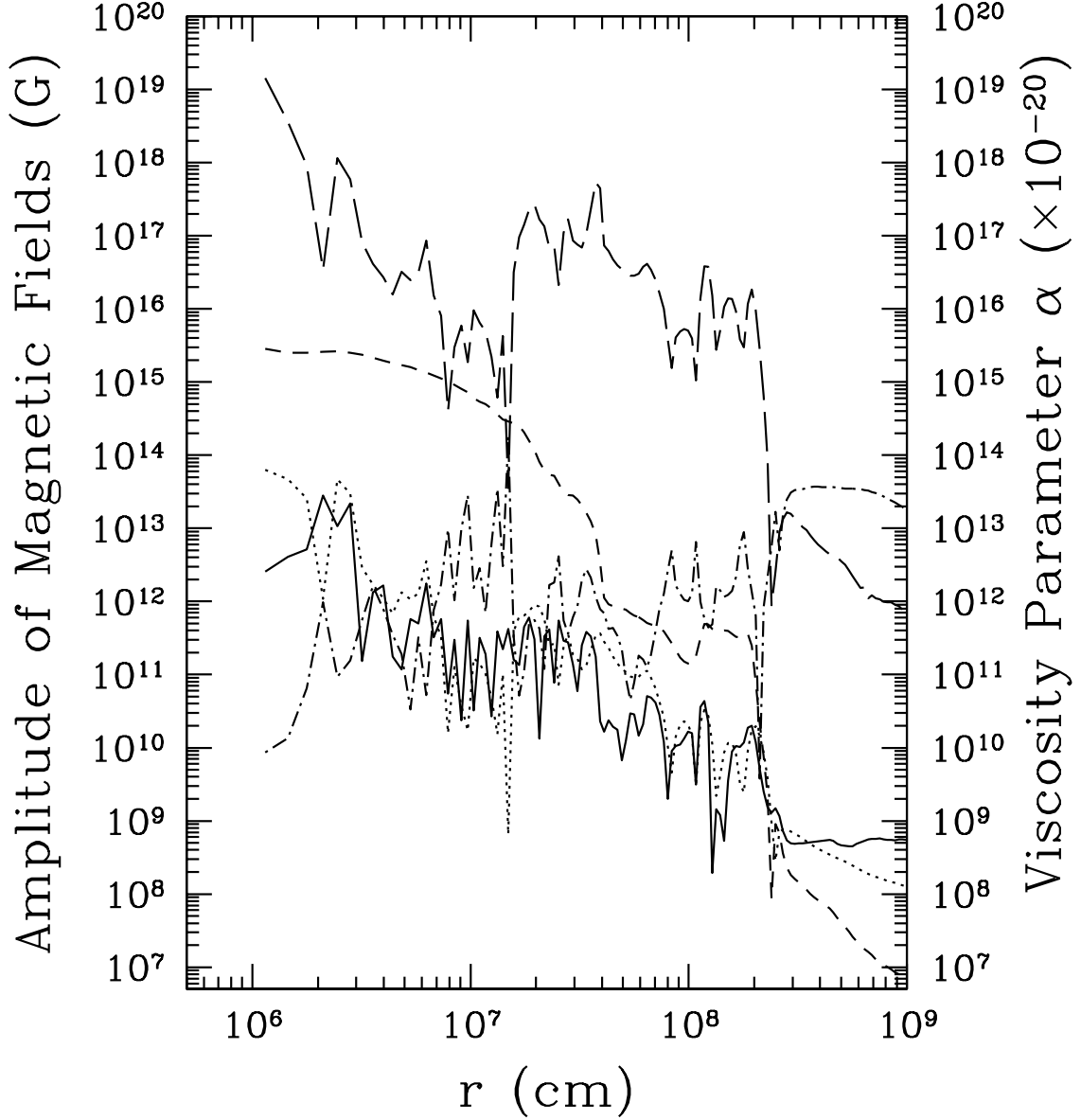


Fig. 11.— Profile of amplitude of magnetic fields and estimated viscosity parameter α ($\times 10^{-20}$) on the equatorial plane for model 9 at $t = 2.2$ s. Dotted, solid, and short-dashed lines represent the amplitude of B_r , B_θ , and B_ϕ , while long-dashed line represent the estimated viscosity parameter. Dot-dashed line represents the Alfvén Mach number ($\times 10^{-10}$) in the radial direction.

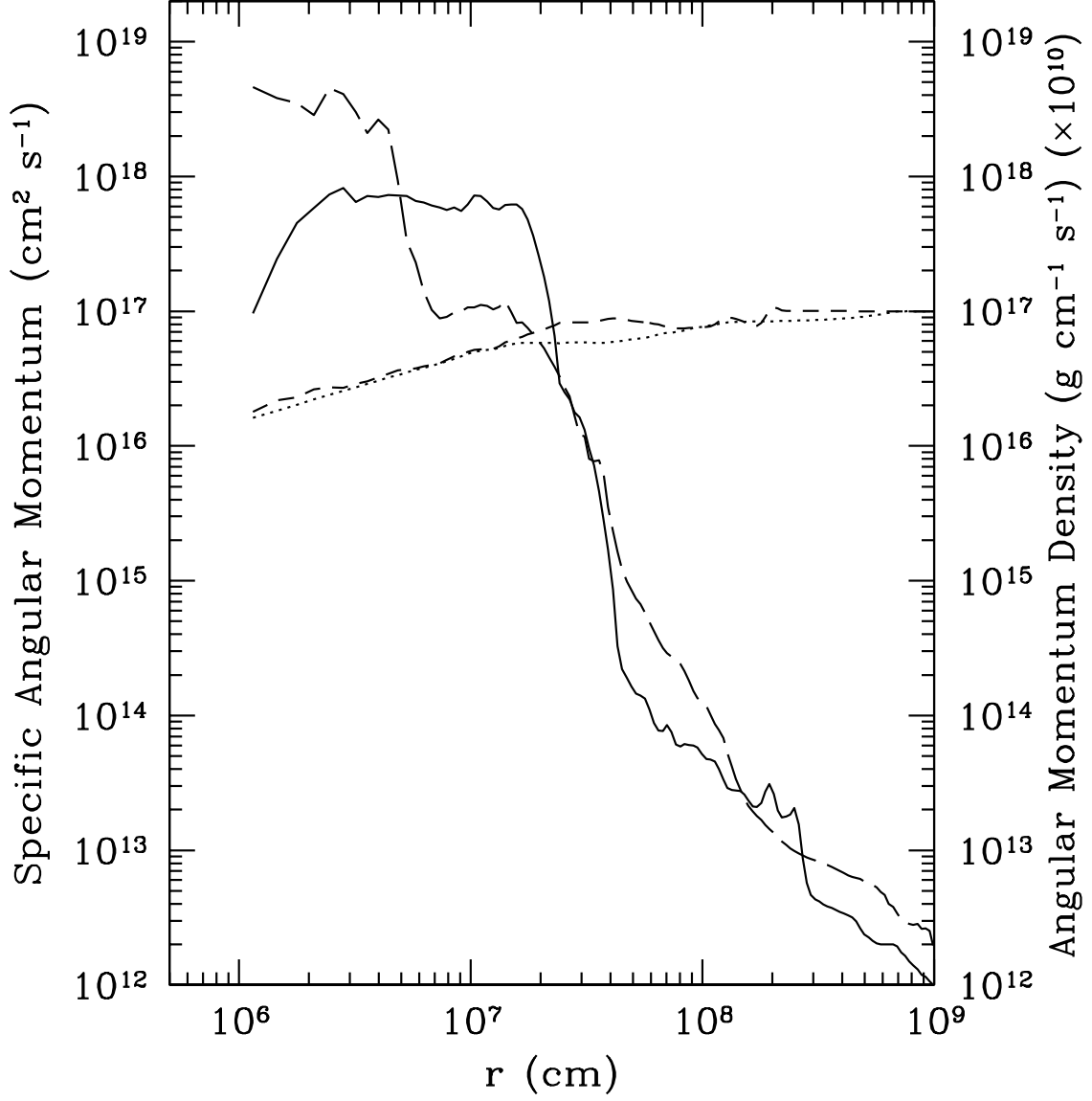


Fig. 12.— Profiles of angular momentum density ($\text{g cm}^{-1} \text{s}^{-1}$) for model 0 (long-dashed line) and model 9 (solid line) on the equatorial plane at $t = 2.2$ s. Profiles of specific angular momentum ($\text{cm}^2 \text{s}^{-1}$) are also shown for model 0 (dotted line) and model 9 (short-dashed line).

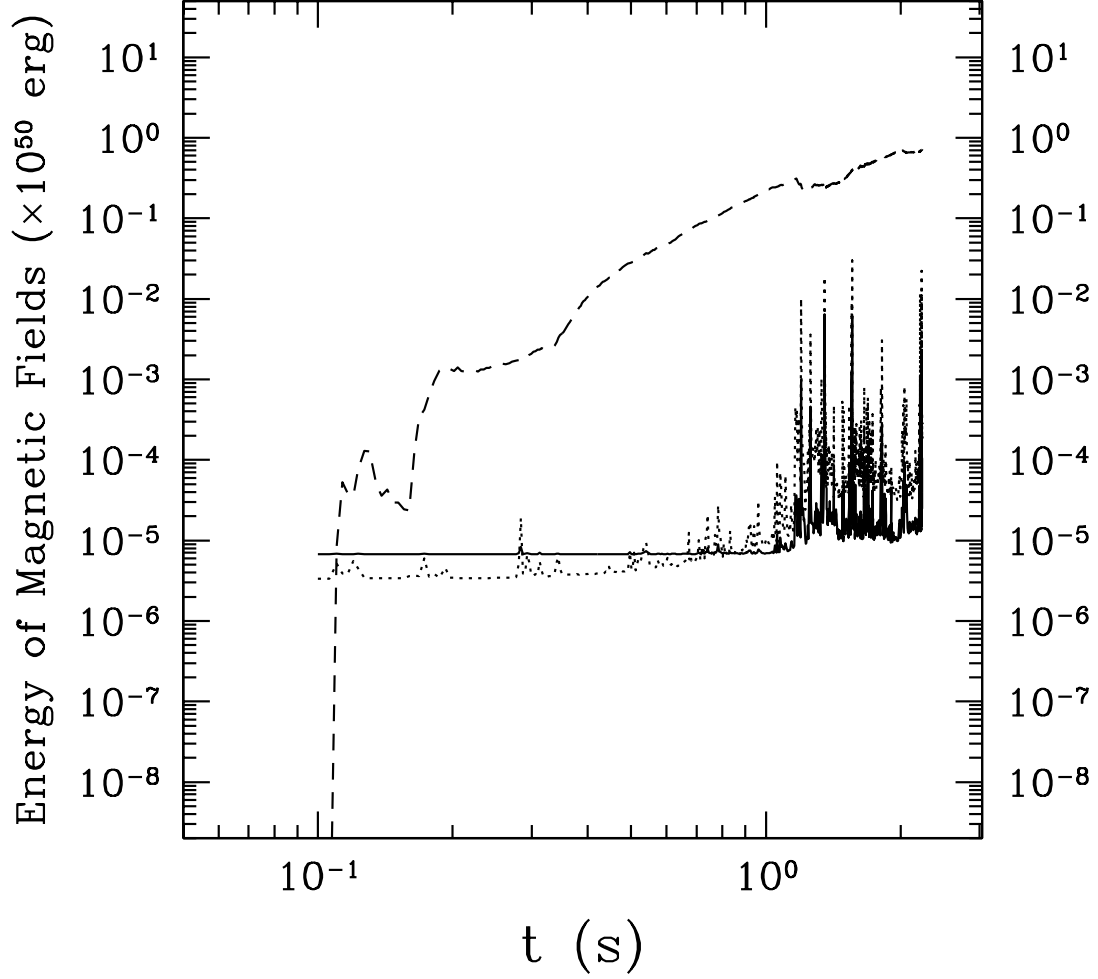


Fig. 13.— Evolution of total energy of magnetic fields ($\times 10^{50}$ erg) for the case of model 9. Dotted, solid, and dashed lines represent energy in the form of B_r , B_θ , and B_ϕ , respectively. Note that 1-D simulation of the spherical collapse of the progenitor is done until $t = 0.1$ s (see Section 2.2), so B_ϕ is set to be 0 until $t = 0.1$ s.

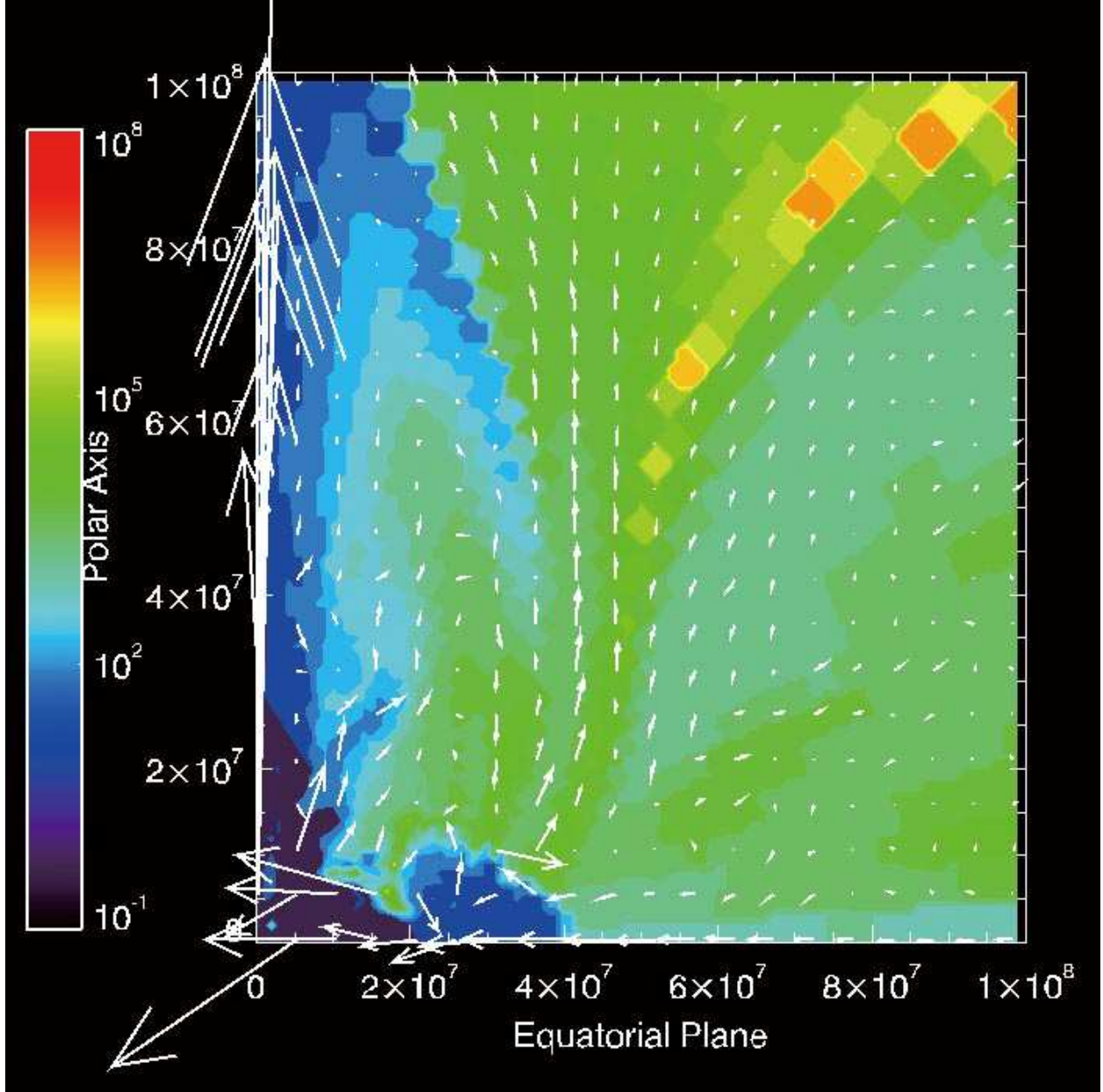


Fig. 14.— Contour of plasma beta ($=p_{\text{gas}+\text{radiation}}/p_{\text{mag}}$) with magnetic fields (B_r and B_θ) for model 9 at $t = 2.2$ s. The color represents the plasma beta in logarithmic scale ($10^{-1} - 10^8$).

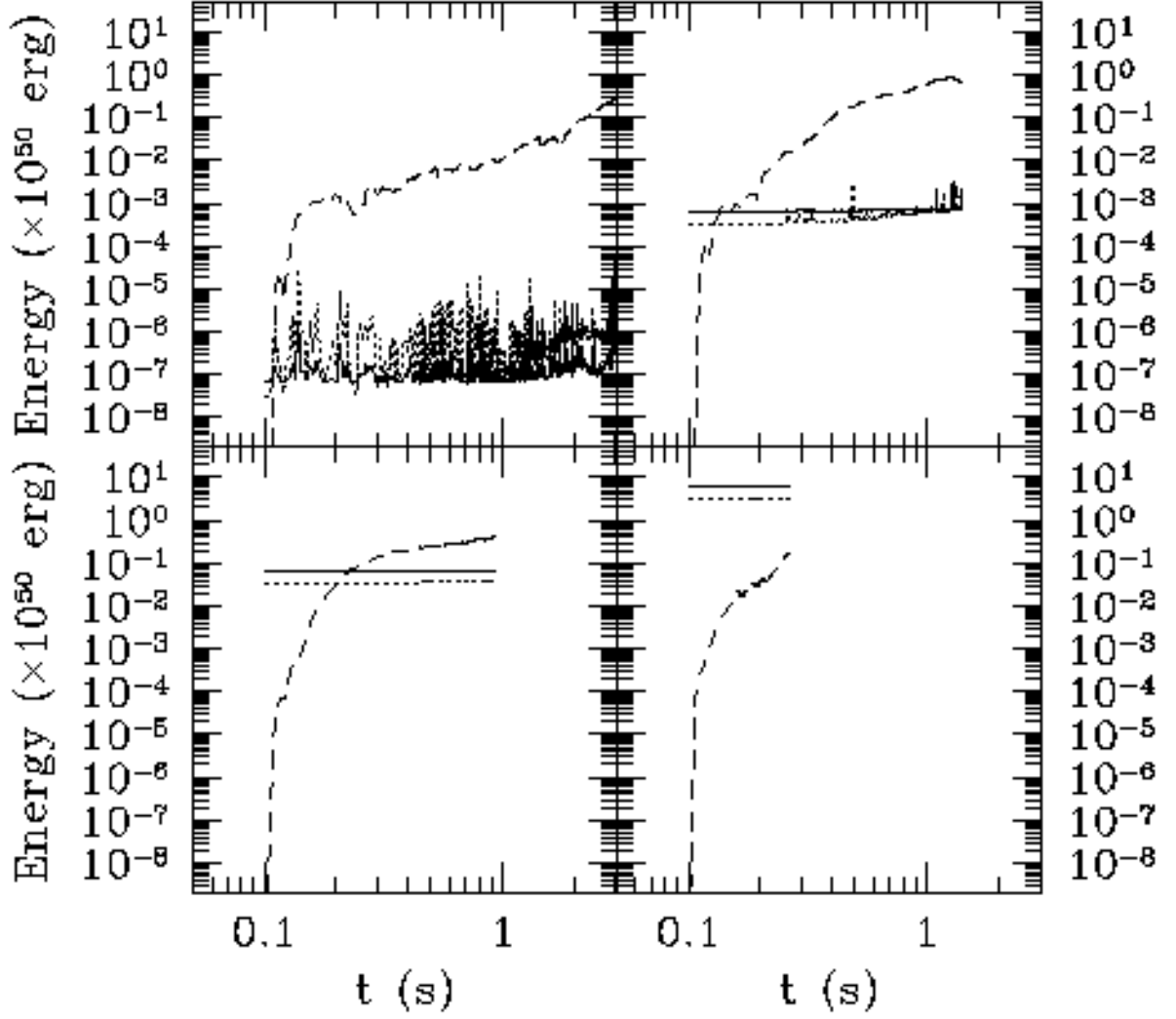


Fig. 15.— Same as Fig. 13, but for model 8 (top-left panel), model 10 (top-right panel), model 11 (bottom-left panel), and model 12 (bottom right panel).

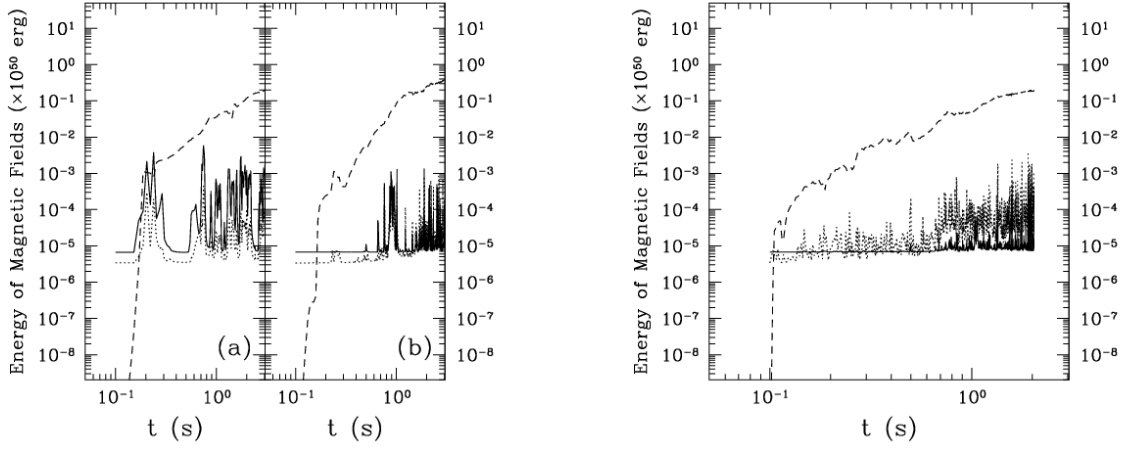


Fig. 16.— Left panel: Same as Fig. 13, but for $150(r) \times 5(\theta)$ grid points (a) and $150(r) \times 20(\theta)$ grid points (b). Right panel: Same as Fig. 13, but for $300(r) \times 60(\theta)$ grid points. In this simulation, neutrino anti-neutrino pair annihilation effect is not included to save CPU time. Simulation region is $(10^6 \text{ cm} \leq r \leq 10^9 \text{ cm}; 0 \leq \theta \leq 90)$.

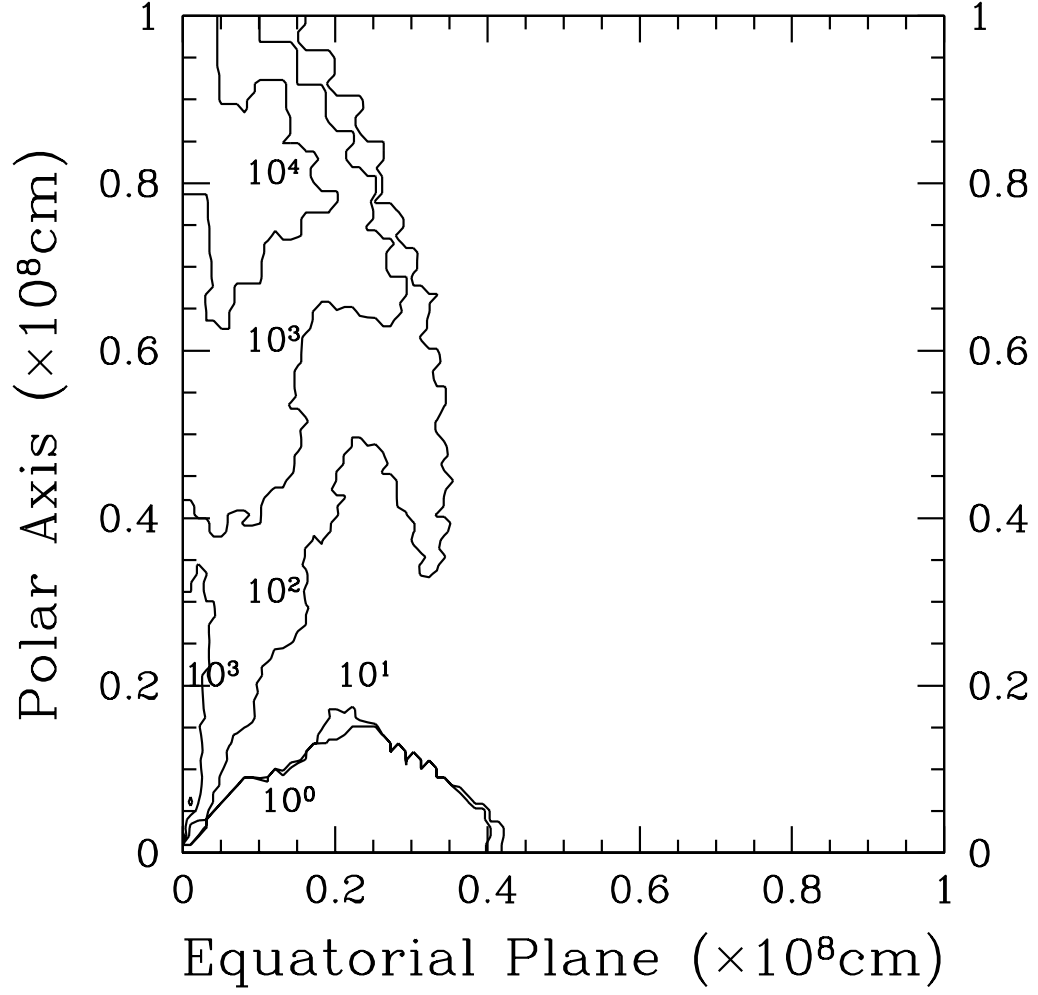


Fig. 17.— Contour of entropy per baryon in units of k_b at $t = 2.2$ s for model 9. The range of the contour is from 1 to 10^5 .

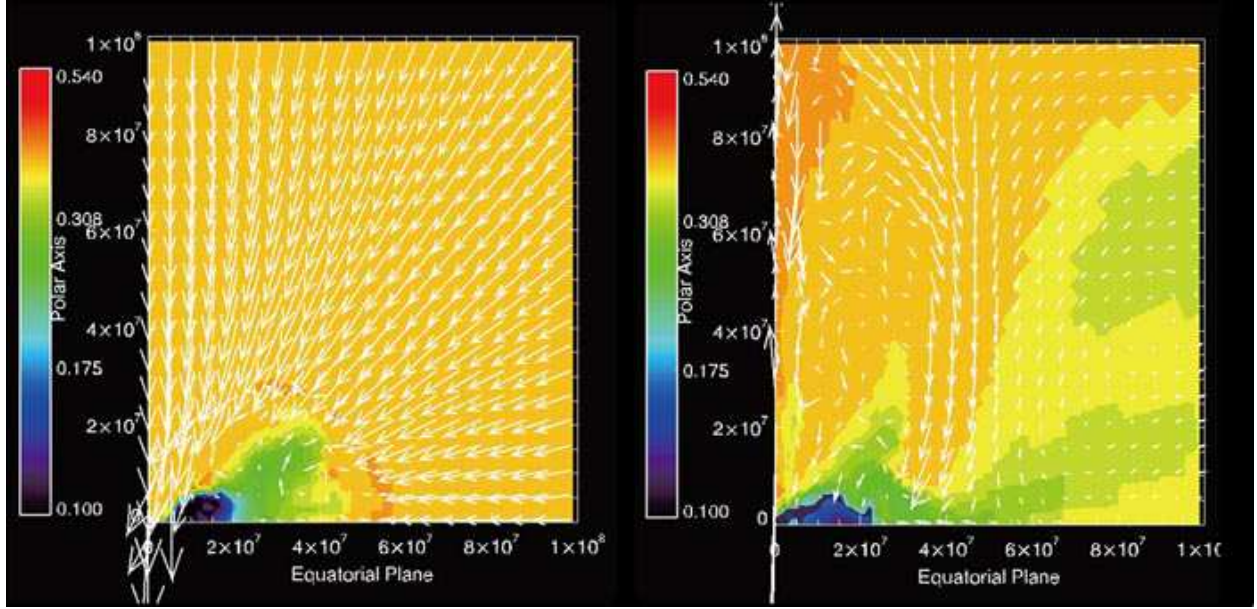


Fig. 18.— Contour of electron fraction with velocity fields for for model 0 at $t = 2.2$ s (left panel) and model 9 at $t = 2.2$ s (right panel). The color represents the electron fraction on a linear scale (0.1-0.540).

Model	$\ T/W\ $ (%)	$\ E_m/W\ $ (%)	B_0 (G)
Model 0	1.3	0	0
Model 8	1.3	1.1×10^{-8}	10^8
Model 9	1.3	1.1×10^{-6}	10^9
Model 10	1.3	1.1×10^{-4}	10^{10}
Model 11	1.3	1.1×10^{-2}	10^{11}
Model 12	1.3	1.1	10^{12}

Table 1: $\|T/W\|$: Initial ratio of the rotational energy to the gravitational energy. $\|E_m/W\|$: Initial ratio of the magnetic energy. B_0 is the strength of the magnetic field in the sphere ($r < 3.6 \times 10^9 \text{cm}$). The digit in the name of each model represents the power index of B_0 .

Model	E_J (erg)	M_J (M_\odot)	Γ^f -1	E_J^{mag}/E_J
Model 8 ($\theta_J = 5^\circ$)	6.97E+47	4.88E-6	7.98E-2	4.75E-2
Model 8 ($\theta_J = 10^\circ$)	7.40E+47	5.39E-6	7.67E-2	5.36E-2
Model 8 ($\theta_J = 15^\circ$)	7.66E+47	5.56E-6	7.70E-2	6.12E-2
Model 9 ($\theta_J = 5^\circ$)	2.96E+47	2.42E-7	6.81E-1	4.71E-2
Model 9 ($\theta_J = 10^\circ$)	4.27E+47	3.13E-7	7.60E-1	3.60E-1
Model 9 ($\theta_J = 15^\circ$)	4.87E+47	4.38E-7	6.21E-1	3.45E-2
Model 10 ($\theta_J = 5^\circ$)	8.17E+45	1.97E-8	2.32E-1	2.83E-1
Model 10 ($\theta_J = 10^\circ$)	9.08E+45	2.12E-8	2.39E-1	2.72E-1
Model 10 ($\theta_J = 15^\circ$)	1.32E+46	3.65E-8	2.03E-1	2.13E-1
Model 11 ($\theta_J = 5^\circ$)	1.05E+48	1.16E-5	5.05E-2	2.74E-1
Model 11 ($\theta_J = 10^\circ$)	1.16E+48	1.24E-5	5.22E-2	2.56E-1
Model 11 ($\theta_J = 15^\circ$)	1.32E+48	1.36E-5	5.44E-2	2.33E-1
Model 12 ($\theta_J = 5^\circ$)	1.45E+49	1.16E-4	6.99E-2	1.69E-1
Model 12 ($\theta_J = 10^\circ$)	1.77E+49	1.52E-4	6.50E-2	1.57E-1
Model 12 ($\theta_J = 15^\circ$)	2.39E+49	2.47E-4	5.42E-2	1.29E-1

Table 2: E_J (erg), M_J (M_\odot), Γ^f , and E_J^{mag}/E_J are mass, total energy, terminal bulk Lorentz factor, and ratio of the magnetic energy relative to total energy of the jet at the final stage of the simulations, respectively. θ_J is the assumed opening angle of the jet. See section 3.3.1 for details.

Model	$M_{\text{Ni}}^{\text{esc}} (M_{\odot})$	$M_{\text{Ni}}^{\text{tot}} (M_{\odot})$
Model 8	6.04E-10	3.79E-3
Model 9	7.52E-11	5.92E-3
Model 10	1.09E-7	3.95E-3
Model 11	1.40E-6	1.61E-3
Model 12	5.62E-7	1.12E-3

Table 3: $M_{\text{Ni}}^{\text{esc}} (M_{\odot})$ and $M_{\text{Ni}}^{\text{tot}} (M_{\odot})$ represent the mass of ^{56}Ni in the regions where total energy (i.e. summation of kinetic energy, thermal energy, and gravitational energy) is positive and the total mass of ^{56}Ni in the whole simulated region at the final stage of the simulations, respectively.